Improved representation of aerosols for HadGEM2

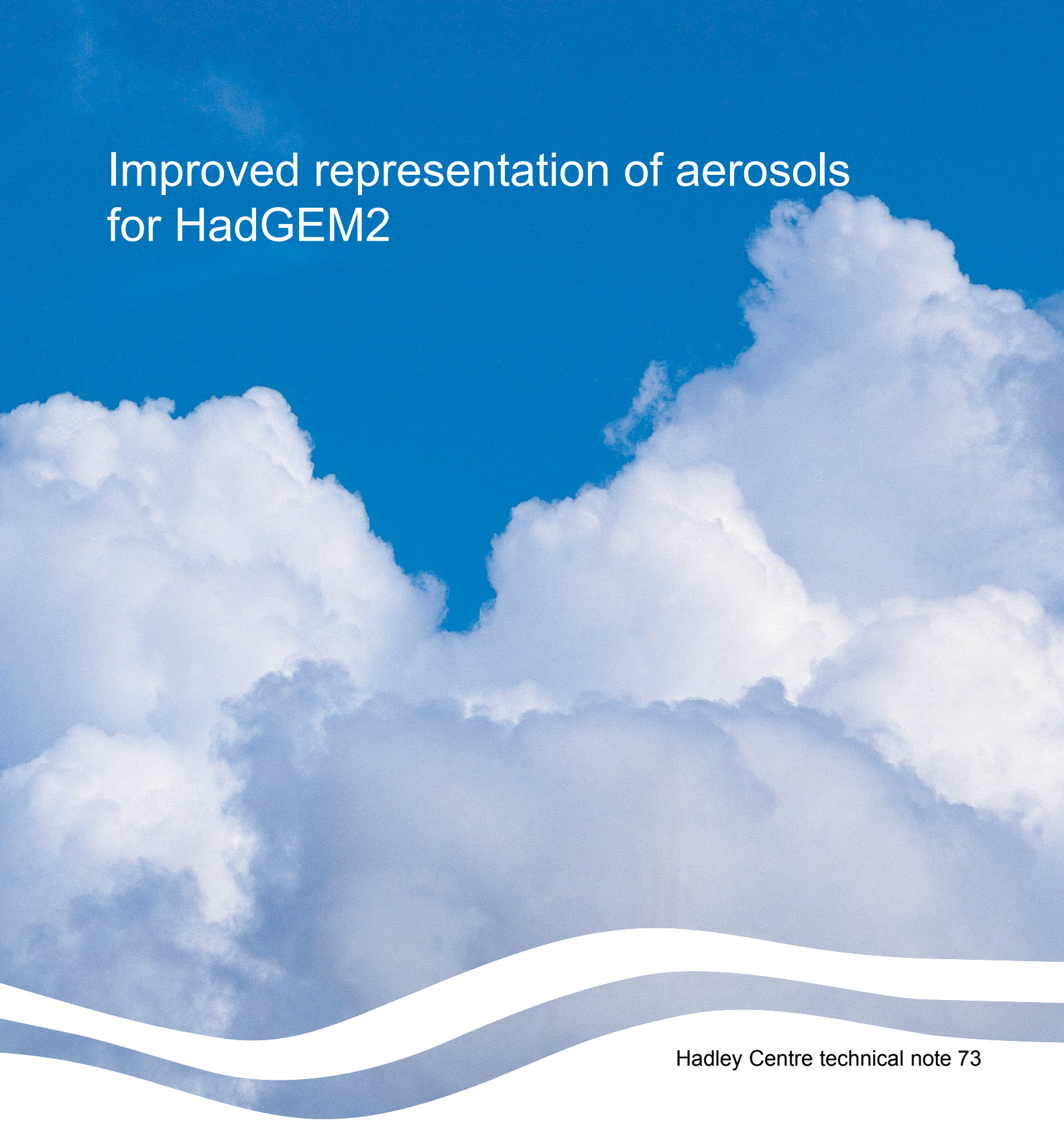

Hadley Centre technical note 73

Nicolas Bellouin, Olivier Boucher, Jim Haywood, Colin Johnson, Andy Jones, Jamie Rae, Stephanie Woodward

March 2007

Met Office

Improved representation of aerosols for HadGEM2

Nicolas Bellouin, Olivier Boucher, Jim Haywood, Colin Johnson, Andy Jones, Jamie Rae, and Stephanie Woodward

March 2007

Climate, Chemistry and Ecosystems
Met Office Hadley Centre for Climate Change
Exeter, Devon, United Kingdom

Abstract

As part of the efforts to improve the physics of the Hadley Centre climate model for the upcoming new version HadGEM2, atmospheric aerosol modelling has been reviewed and significantly improved. This process includes revised sulphur cycle and biomass burning representations. These translate into an increased magnitude of the negative aerosol radiative forcing with respect to pre-industrial conditions, by 30% from changes to sulphate modelling, and 15% from improvements to the biomass-burning scheme. Mineral dust and secondary organic aerosols, absent from the previous version of the climate model, HadGEM1, are now introduced. When those changes are included, model simulations improve significantly, agree reasonably with aerosol observations and are in line with comparable global aerosol models.

Contents

1 Introduction

Aerosols interact with solar and thermal radiation through scattering and absorption (direct effect) and changes in cloud microphysics (indirect effects) [Ramaswamy *et al.* 2001]. These effects are quantified using their perturbation to shortwave and longwave radiative fluxes at the top of the atmosphere. Aerosols released into the atmosphere by human activities exert a forcing on the climate system. On a global average, this forcing is negative, thus offsetting parts of the positive forcing due to greenhouse gases. Locally however, the forcing can be positive, adding a warming component. The sign of the forcing is a function of aerosol absorption and underlying surface reflectance (or brightness). Stott *et al.* [2000] showed that the radiative effects of both natural and anthropogenic aerosols must be included in a climate model in order to reproduce the temperature trends of the 20^{th} century. An accurate estimate of the aerosol perturbation is also needed to minimise the uncertainties in assessing the climate sensitivity and future climate change. It has been shown that the uncertainty in the climate sensitivity to a doubling of the CO_2 concentration is related to the uncertainty in the present-day aerosol forcing (although other forcings must also be taken into account) [Andreae *et al.* 2005].

Simulating the total aerosol radiative perturbation is not trivial. Modelled aerosols must be described by the right loading at the correct geographical locations. The way they interact with radiation and act as cloud condensation nuclei must also be well parameterised. These aspects are difficult to validate concurrently and on a global scale. Fortunately, satellite and ground-based instruments dedicated to aerosol studies haven been deployed in the 1990s and have operated since then. They measure, on a daily basis and covering most of the cloud-free surface of the Earth, the aerosol optical depth, which quantifies the wavelength-dependent extinction of radiation due to aerosols. The aerosol optical depth is a valuable validation tool as both the aerosol loading and optical properties are included in a single quantity. Unfortunately, cloudy skies make aerosol observations difficult, and neither the direct effect in cloudy skies nor the indirect effect are presently observed. Nevertheless, successfully comparing the modelled against the observed aerosol optical depths increases the confidence in the modelled aerosol direct radiative forcing.

The Hadley Centre Global Environmental Model version 1 (HadGEM1) and specifically its atmospheric component, HadGAM1, include representations of sulphate, black-carbon (also termed soot), sea-salt and biomass-burning aerosols. For the next version, HadGEM2, several changes and additions have been made and are detailed in this document. Before considering changes to the aerosol schemes themselves, section 2 presents changes made to the interaction with radiation and the addition of aerosol optical depth diagnostics. Section 3 lists the deficiencies identified in the existing schemes and changes made to address those deficiencies. Section 4 introduces two new aerosol species, mineral dust and secondary organic aerosols, that were missing in HadGEM1 and have been added for HadGEM2. The impact of those changes on the simulated aerosol radiative perturbation is discussed in section 5. Comparisons against satellite and ground-based instruments are shown in section 6.

2 Changes made to the interaction with radiation

Aerosols scatter and absorb incoming shortwave radiation (solar spectrum) and, to a lesser extent for most species, outgoing longwave radiation (terrestrial spectrum). The scattering is maximal when the aerosol size is comparable to the wavelength. In the visible spectrum, aerosols smaller than 0.5 μm in radius (called accumulation-mode aerosols) are most efficient. The sum of the scattering and absorption is called the extinction. The extinction efficiency, measured by the specific extinction coefficient, k_{ext} (m^2kg^{-1}), depends on the wavelength. This coefficient is computed assuming aerosols are spherical and using Mie scattering calculations, based on a prescribed size distribution and wavelength-dependent refractive indices.

2.1 Aerosol optical depth diagnostics

The extinction aerosol optical depth, noted τ_{ext} or more often simply τ, is the column-integrated extinction, defined as

$$\tau(\lambda) = \int_z k_{\text{ext}}(\lambda) r(z) \rho(z) dz \tag{1}$$

where λ is the wavelength, z is the vertical coordinate (in m), k_{ext} is the specific extinction coefficient (m^2kg^{-1}), r is the aerosol mass mixing ratio (kg kg^{-1}) and ρ is the air density (kg m^{-3}). The aerosol optical depth is dimensionless and typically ranges between 0 and 3, with an observed global mean of about 0.15 at 0.55 μm. It is also possible to define an optical depth for scattering (τ_{sca}) by simply using the specific scattering coefficient in equation 1, and an optical depth for absorption (τ_{abs}) by using the specific absorption coefficient. Following the definition of the extinction, those two quantities verify

$$\tau_{\text{sca}} + \tau_{\text{abs}} = \tau_{\text{ext}} \tag{2}$$

and are used when defining the single-scattering albedo, ϖ_0, as:

$$\varpi_0 = \frac{\tau_{\text{sca}}}{\tau_{\text{sca}} + \tau_{\text{abs}}} = \frac{\tau_{\text{sca}}}{\tau_{\text{ext}}} \tag{3}$$

The single-scattering albedo therefore gives the fraction of the extinction that is due to scattering and, conversely, is a measure of the importance of the aerosol absorption. An aerosol with $\varpi_0 = 1$ is purely scattering. This is typically the case of sea salt and sulphate aerosols in the solar spectrum. In contrast, a strongly absorbing aerosol, such as black carbon, can have a value as low as 0.4. The value of the single-scattering albedo is important as there exists a "critical single-scattering albedo" [King *et al.* 1999]. Below that critical value, an aerosol will exert a positive radiative perturbation (warming) in a fashion more or less independent of its optical depth. This lower threshold depends on the underlying surface reflectance (or brightness). The brighter the surface, the larger the critical single-scattering albedo: it is therefore easier to have positive radiative perturbations over bright surfaces such as deserts, ice-covered areas, and clouds.

As stated in the introduction, the aerosol optical depth is a useful diagnostic, but is not available in HadGEM1. It has been added to HadGEM2, providing the aerosol optical depth at six wavelengths, chosen to match those commonly used by remote-sensing instruments. These are 0.38, 0.44, 0.55, 0.67, 0.87 and 1.02 μm.

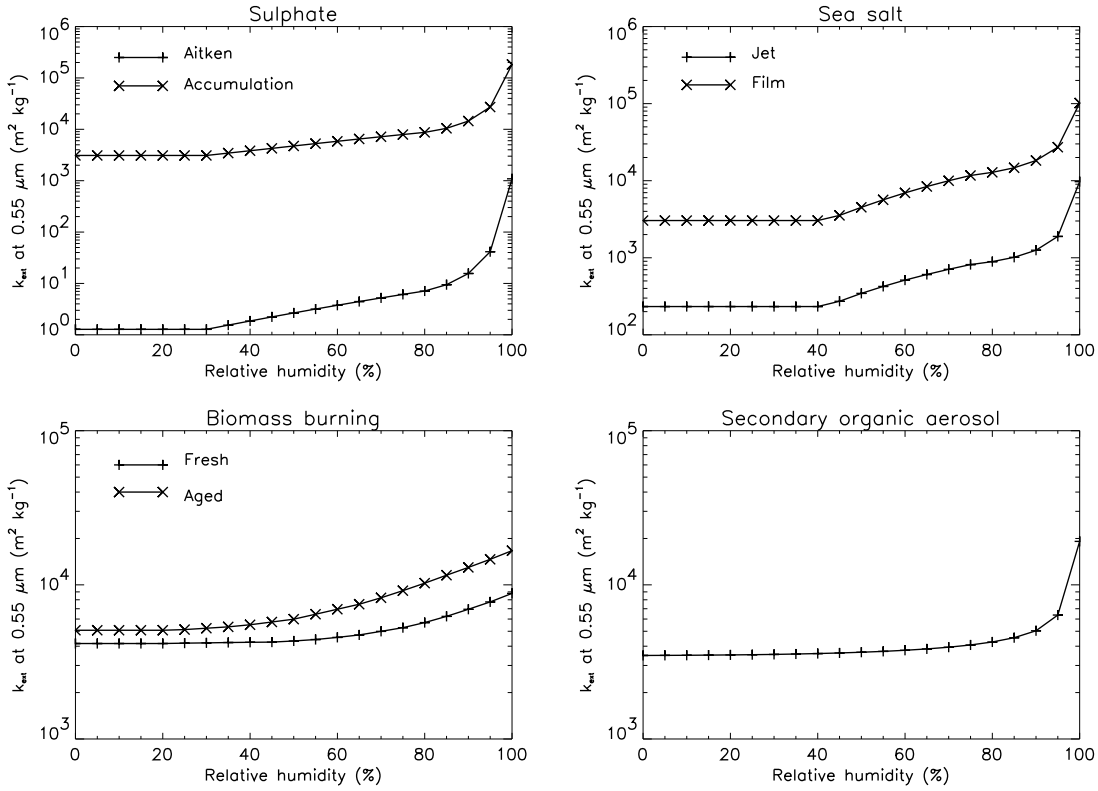

Figure 1: Specific extinction coefficients at 0.55 μm for HadGEM2's hygroscopic aerosols as a function of relative humidity.

2.2 Relative humidity and hygroscopic growth

Some aerosols species are hygroscopic. It means their size grows due to uptake of water vapour and their refractive index is modified by that of water. Consequently, their specific extinction coefficient increases with relative humidity. This increase is typically several orders of magnitude between the dry (relative humidity of 0%) and moist (relative humidity of 100%) aerosol. Consequently, a moist aerosol will have a larger optical depth and exert larger radiative perturbations than its dry counterpart. Figure 1 shows the specific extinction coefficient at 0.55 μm for the aerosol types that are hygroscopic in HadGEM2. Note the logarithmic scale of the vertical axis. Sulphate and sea salt aerosols hygroscopic growth is modelled following Fitzgerald [1975]. The hygroscopic growth of biomass-burning and secondary organic aerosols is a new feature of HadGEM2, and is described in sections 3.2.3 and 4.1, respectively.

As the specific extinction coefficient varies greatly with relative humidity, it is important to determine what relative humidity is actually experienced by aerosols in clear-sky conditions. In HadGEM1, the grid-box mean relative humidity is used. It is biased towards larger values when clouds are present and is therefore not representative of clear-sky conditions. In HadGEM2, the grid-box mean RH has therefore been replaced by the clear-sky mean relative humidity to address this bias. This clear-sky mean relative humidity is computed by first calculating the clear-sky water vapour

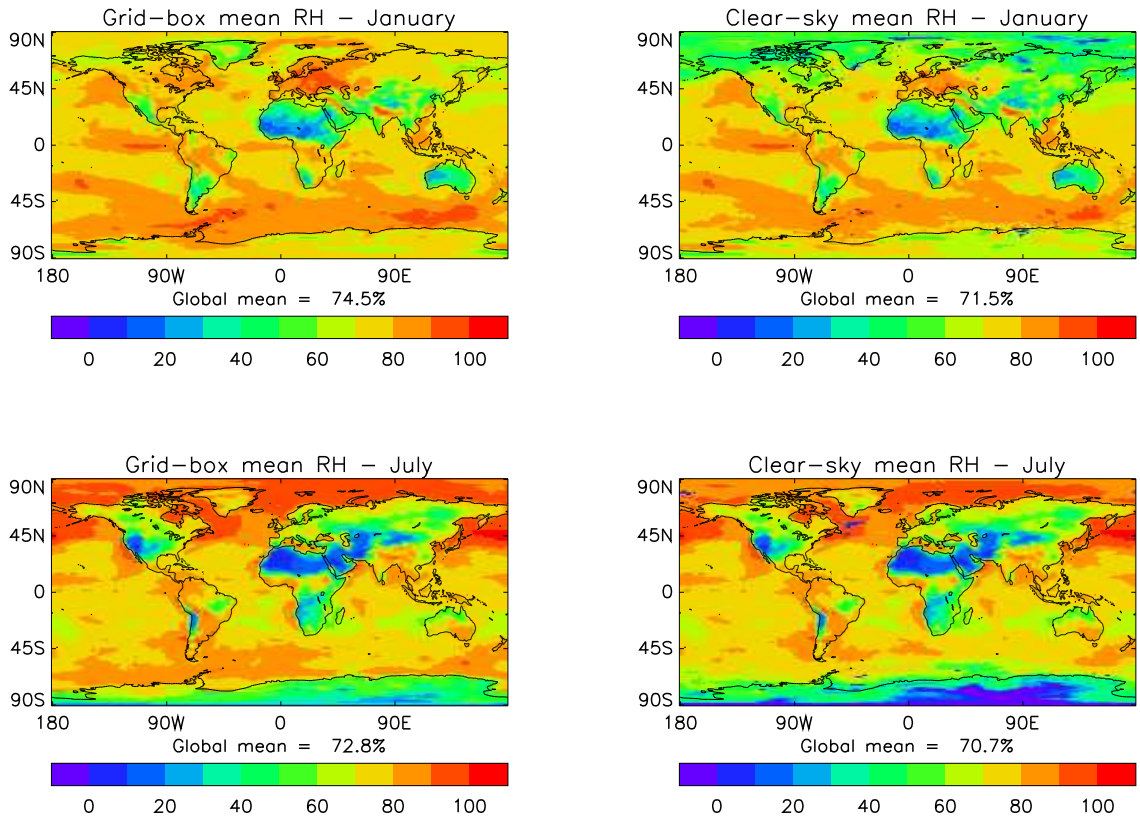

Figure 2: Comparison of the monthly-averaged grid-box mean relative humidity (left) against the clear-sky mean relative humidity (right) for the months of January and July.

mixing ratio, $w_{\rm clr}$ as:

$$w_{\rm clr} = \frac{(w - CCw_{\rm sat})}{(1 - CC)} \tag{4}$$

where w is the total water vapour mixing ratio of the grid-box and $w_{\rm sat}$ is the saturated water vapour mixing ratio. The latter is a function of temperature and pressure. CC is the fractional cloud cover. Equation 4 is built from two common assumptions. First, the mixing ratio of clouds is assumed to be the saturated mixing ratio (*i.e.* condensation is instantaneous). Second, temperature and pressure are assumed not to be distributed across the grid-box. When the cloud fraction is 1, $w_{\rm clr}$ is undefined and is assumed to be 0. After determining the clear-sky water vapour mixing ratio, the clear-sky relative humidity ($RH_{\rm clr}$ in %) is simply given by:

$$RH_{\rm clr} = \frac{w_{\rm clr}(1 - w_{\rm sat})}{w_{\rm sat}(1 - w_{\rm clr})} \times 100 \tag{5}$$

Figure 2 shows the modelled grid-box mean and clear-sky mean relative humidities for January and July at the lowest atmospheric level. As expected, the relative humidity computed in the clear-sky part of the grid-box is smaller than that computed across the entire grid-box. Land surfaces in the winter and high latitude oceans show the largest differences between these two relative humidities.

3 Changes made to the existing aerosol schemes

3.1 Sulphur cycle

3.1.1 Introduction

The version of the sulphur cycle included in HadGEM1 is described in Jones *et al.* [2001] and Roberts and Jones [2004]. It is a modal scheme where the free aerosol is assumed to have a log-normal size distribution in the Aitken and accumulation size ranges, which include particles with a radius less than 0.05 and 0.5 μm, respectively. Accumulation-mode aerosols, having sizes comparable to shortwave wavelengths, are the most optically efficient and therefore important when considering the aerosol direct perturbation. Sulphate aerosol may also be in a dissolved mode where layer clouds are present, thus affecting the cloud droplet size and exerting indirect effects. In HadGEM1, the sulphur cycle places only 22% of the non-dissolved sulphate mass (0.5 Tg[S]) into the accumulation mode. This is not supported by observations and other models, where the situation is actually reversed: the majority of the sulphate mass should lie in the accumulation mode. To correct for this, three processes have been identified which need improvement or are missing in HadGEM1. Firstly, the loss of dissolved mode sulphate during large-scale precipitation is too large, due to not accounting for re-evaporation. Secondly, the condensation of sulphuric acid from the dry oxidation of sulphur dioxide and dimethylsulphide is inadequately described. Thirdly, the process by which Aitken-mode particles grow by condensation to become accumulation-mode particles is missing. The parameters of the log-normal distribution describing sulphate aerosols are also modified and the effect of sulphate on cloud droplet sizes is updated to account for these improvements. In the following, we review these changes in turn and assess their impact.

3.1.2 Re-evaporation of precipitation

Aerosols dissolved in cloud droplets, such as sulphate aerosols, are removed from the atmosphere during large-scale precipitation, a process called rainout. In HadGEM1, the scheme removes from each layer an amount of dissolved aerosol proportional to the amount of condensed water removed as precipitation (as rain or snow). This does not take into account the re-evaporation of precipitation, *i.e.* precipitation from higher layers evaporating before reaching the surface. In HadGEM1, approximately a quarter of the large-scale precipitation evaporates. In HadGEM2, the scheme is modified with a different computation of the amount that is rained out and to account for re-evaporation. Re-evaporation is assumed to transfer mass from the dissolved to the accumulation mode.

In each model layer, the net precipitation flux (ΔF in $\mathrm{kgm^{-2}s^{-1}}$) is defined as

$$\Delta F = F_{\mathrm{out}} - F_{\mathrm{in}} \tag{6}$$

and is given by the cloud scheme. F_{out} is the flux falling out of the bottom of the layer on which it is defined, and F_{in} is the flux falling into that layer (or, equivalently, the flux falling out of the layer above). Re-evaporation occurs if ΔF is negative, whereas a positive ΔF means in increase in precipitation.

The conversion rate of cloud water into precipitated water, noted β and given in s^{-1}, is computed as:

$$\beta = \frac{\Delta F}{\rho_{\text{air}}\ Q} \tag{7}$$

where ρ_{air} is the density of air (kg of air per unit volume) and Q is the cloud liquid and frozen water content before large-scale precipitation, in kg per kg of air. β is a positive quantity. The amount of rained out aerosol mass mixing ratio (Δr in kg kg^{-1}) is given by:

$$\Delta r = r\ \ [\exp(-\beta t) - 1] \tag{8}$$

where r is the aerosol mass mixing ratio (kg kg^{-1}) and t is the length of a model timestep, in seconds. By definition, Δr is negative or zero. For each model layer, the accumulated rain-out (kgm^{-2}) is computed as

$$\sum_{i}^{\text{top}} \Delta r(i)\rho_{\text{dry}}(i) \tag{9}$$

where i denotes the current model layer.

To account for re-evaporation, the fraction of precipitated water that evaporates, γ, is computed as

$$\gamma = \frac{\Delta F}{F_{\text{in}}} \tag{10}$$

If γ equals 1 (or, equivalently, if F_{out} is zero), the re-evaporation is total and the whole accumulated rain-out, as computed following equation 9, is added to the accumulation-mode mass mixing ratio. If the re-evaporation is not total, a fraction is introduced to represent those raindrops that shrink without re-evaporating. This fraction, f_{shrink}, isn't well constrained by observation, and is given an arbitrary value of 0.5. The accumulation-mode mass mixing ratio therefore receives a re-evaporated contribution equal to

$$\gamma\ f_{\text{shrink}}\ \frac{\sum_{i}^{\text{top}} \Delta r(i)\rho_{\text{dry}}(i)}{\rho_{\text{dry}}} \tag{11}$$

The accumulated rainout is corrected for the amount that re-evaporated, in order to conserve aerosol mass.

Although originally designed for sulphate aerosols, the improved rainout scheme has been extended to all other prognostic aerosols having a dissolved or in-cloud mode, namely biomass-burning and black carbon aerosols, for the sake of consistency. For those aerosols, the re-evaporated amount is transferred to the aged mode.

3.1.3 Condensation of sulphuric acid and mode merging

The condensation of sulphuric acid (H_2SO_4) onto pre-existing aerosol may be described from theory and modelled if an adequate number of aerosol size components can be included. Here we investigate a parameterised approach for: 1) the split in the sulphuric acid deposition between the Aitken and accumulation mode; and 2) the rate of transfer from the Aitken mode to the accumulation mode. The condensation

theory as used in the GLOMAP model [Spracklen *et al.* 2005] was employed to answer these questions. This theory is outlined below, and was parameterised in order to be included as part of the sulphate aerosol model in HadGEM2.

Condensation theory

The loss rate of $[H_2SO_4]$ onto the aerosol is described by the equation:

$$\frac{\mathrm{d}[H_2SO_4]}{\mathrm{d}t} = -CN[H_2SO_4] \tag{12}$$

where N is the number of particles, $[H_2SO_4]$ the gas-phase concentration of sulphuric acid, and C is calculated from:

$$C = 4\pi R_{\mathrm{wet}} DF(Kn)A(Kn) \tag{13}$$

where R_{wet} is the moist radius of the particle, D is the diffusivity of H_2SO_4 in air, and $F(Kn)$ and $A(Kn)$ are functions of the Knudsen number:

$$F(Kn) = \frac{1 + Kn}{1 + 1.71Kn + 1.33Kn^2} \tag{14}$$

$$A(Kn) = \frac{1}{1 + 1.33KnF(Kn)\left(\frac{1}{S_{\mathrm{e}}} - 1\right)} \tag{15}$$

where S_{e} is the sticking efficiency, and the Knudsen number is defined as:

$$Kn = \frac{\lambda}{R_{\mathrm{wet}}} \tag{16}$$

where λ is the mean free path for H_2SO_4 molecules in air.

The diffusivity, D is given by:

$$D = \left(\frac{3}{8\rho_{\mathrm{a}} N_{\mathrm{a}} d_{\mathrm{s}}^2}\right)\left(\frac{RTM_{\mathrm{air}}\left(1 + \frac{M_{\mathrm{air}}}{M_{\mathrm{s}}}\right)}{2\pi}\right)^{0.5} \tag{17}$$

where ρ_{a} is the air density in kg m^{-3}, N_{a} is Avogadro's number, d_{s} the diameter of a molecule of H_2SO_4, and M_{air} and M_{s} are the molecular weights for air and H_2SO_4 respectively. The mean free path for H_2SO_4 is calculated from:

$$\lambda = \left(\frac{M_{\mathrm{s}}}{8N_{\mathrm{a}}^2 d_{\mathrm{s}}^2\, \rho_{\mathrm{m}} M_{\mathrm{a}}}\right)\left(\frac{M_{\mathrm{air}}}{M_{\mathrm{air}} + M_{\mathrm{s}}}\right)^{0.5} \tag{18}$$

where ρ_{m} is the air density in mol m^{-3}, and $\mathrm{M_a}$ is the mass of an air molecule.

Rate of transfer from Aitken to accumulation mode

To calculate the rate of growth of the Aitken mode aerosol into the accumulation mode, the mass transfer per timestep between the two modes needs to be calculated. This was done by calculating the increase in the Aitken mode mass in the region where particle radius is greater than a pre-determined radius. The mass increase in this region is then partitioned into the accumulation mode aerosol. The radius where the two distributions overlap, approximately 7.0×10^{-8} m, was used to determine the

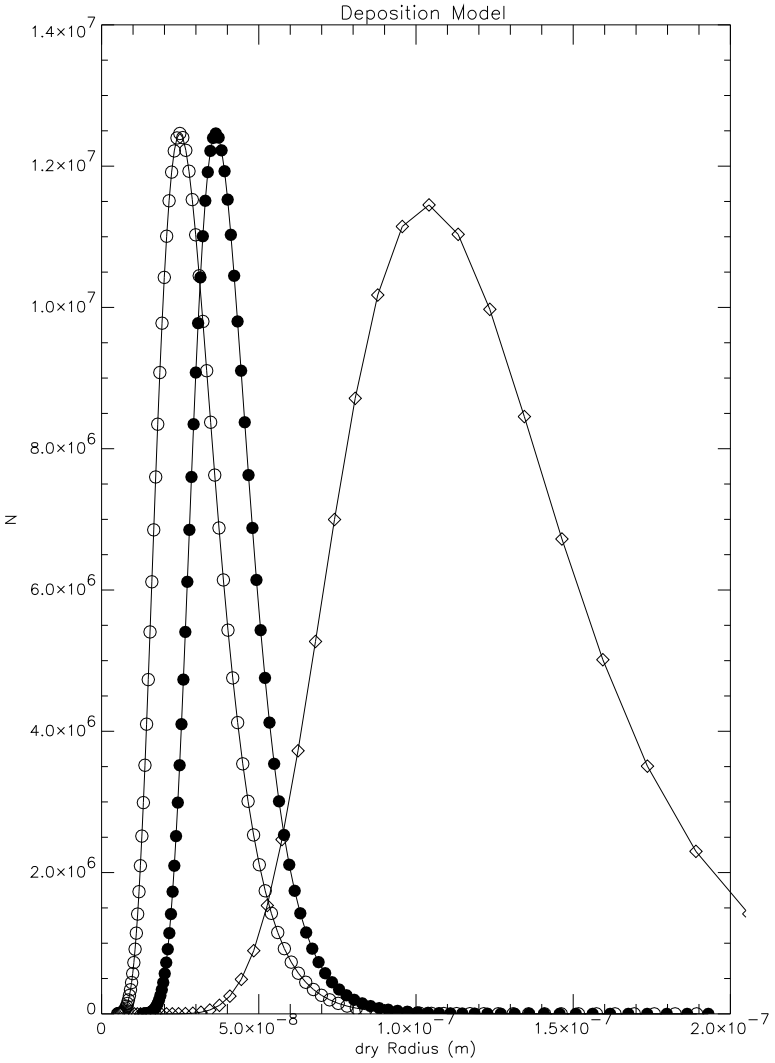

Figure 3: Growth due to deposition of sulphuric acid onto Aitken mode aerosol: initial Aitken mode (○), Aitken mode after timestep (●), accumulation mode (◇).

region concerned. Figure 3 shows the initial and final Aitken mode aerosol number distribution after deposition of H_2SO_4, compared to the accumulation mode aerosol. As more particles are transferred into the overlap region with increasing H_2SO_4 concentrations, the fraction of the Aitken mode which grows into accumulation mode is a non-linear function of $[H_2SO_4]$. Figure 4 shows this curve for three overlap points.

The H_2SO_4 concentration may be calculated by assuming a steady state relationship:

$$k_1[\mathrm{OH}][\mathrm{SO_2}]M_{\mathrm{H_2SO_4}}10^6 = [\mathrm{H_2SO_4}]\sum_{i=1}^{i=n} C_i.N_i \tag{19}$$

with $M_{\mathrm{H_2SO_4}}$ the molecular weight of H_2SO_4, and the factor of 10^6 converts to units of kg m^{-3}. As an example, choosing a SO_2 concentration of 1 ppbv, with an OH concentration of 2×10^6 molecules cm^{-3} gives $[H_2SO_4]$ of 4×10^{-12} kg m^{-3}. This translates into a mass fraction of 0.007 per timestep, equivalent to a 3 day lifetime.

Relative condensation of H_2SO_4 onto Aitken and accumulation mode

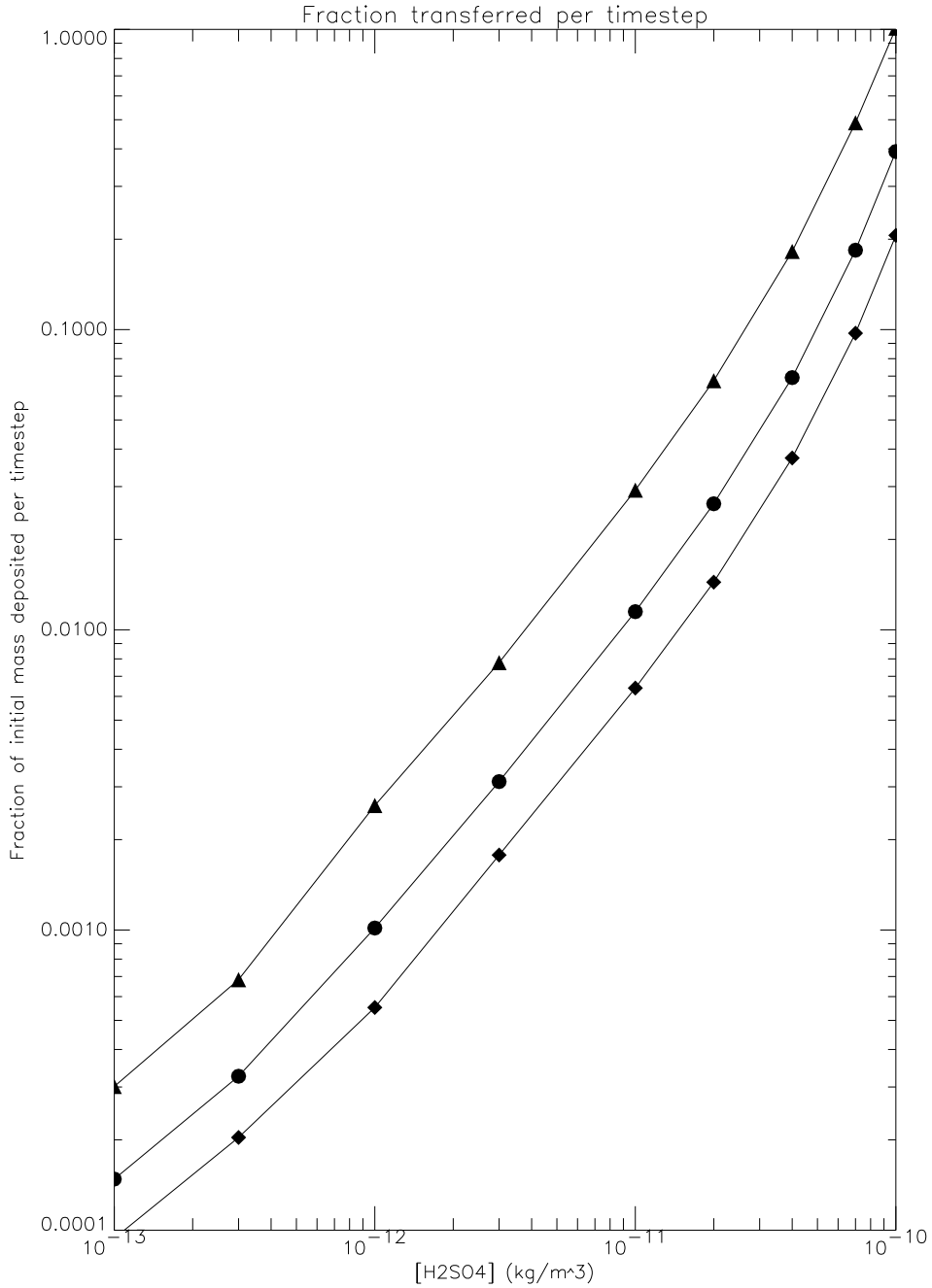

Figure 4: Calculated fraction of the Aitken mode which grows by deposition into accumulation mode as a function of $[H_2SO_4]$. The results for three overlap radii are shown: 7.0×10^{-8} m (●), 7.6×10^{-8} m (◇), and 6.05×10^{-8} m (△).

aerosol

In the previous section we assumed that all the condensation was to the Aitken mode aerosol. However there will also be condensation to the accumulation mode, and the fraction of the condensate to the accumulation mode is calculated from:

$$F = \frac{\sum_{i=1}^{i=n} Ca_i Na_i}{\sum_{i=1}^{i=n} CA_i NA_i + \sum_{i=1}^{i=n} Ca_i Na_i} \tag{20}$$

where CA, NA are for the Aitken mode and Ca, Na are for the accumulation mode. From Equation 13, CA and Ca vary with the mass of aerosol and the wet radius, itself a function of the relative humidity. Assuming that the aerosol mass in the Aitken mode is 5% of that in the accumulation mode, then the flux to the accumulation mode will be around 30% of that to the Aitken mode; if the mass in the Aitken mode is 25% of that in the accumulation mode then the fraction will be around 70%. Only where the Aitken mode is a small fraction of the accumulation mode mass can we expect significant deposition to the accumulation mode aerosol, otherwise most of the condensate will be deposited onto the Aitken mode aerosol.

Parameterisation of condensation and mode-merging processes

To avoid excessive CPU costs for this calculation, a parameterisation of these processes has been used in the new scheme. The fraction transferred from the Aitken mode to the accumulation mode at each timestep depends on the pressure, temperature, relative humidity, sulphur dioxide (SO_2) concentration and hydroxide (OH) concentration. However, both concentrations are only used to predict the flux through Equation 19, and the amount transferred is linearly related to this flux. The other factors, for example relative humidity, are less important. As a first order parameterisation, the following procedure has been adopted. To predict the condensation split to Aitken and accumulation mode aerosol, Equation 20 is parameterised using a look-up table for the sums of $C.N$ for Aitken and accumulation mode aerosol. These also vary linearly with the aerosol mass. Once the flux to the Aitken mode is known, this can be used to predict the fraction transferred to the accumulation mode assuming all other factors are unimportant. From exact calculations it was found that the fraction transferred to the accumulation mode per timestep (f) was 0.012 with $[SO_2] = 4{\times}10^{10}$ molecules cm^{-3}, $[OH] = 2{\times}10^{6}$ molecules cm^{-3}, $T = 288$ K, $p = 101315$ Pa, and $RH = 0.75$. For these conditions, there is a flux (F) of H_2SO_4 of $1.087{\times}10^{-14}$ kg m^{-3} s^{-1}. In the model, the relevant flux is calculated in terms of mass mixing ratio of sulphur per timestep. The slope of this relationship may be converted to give the fraction of the Aitken mode transferred in terms of the condensation flux to the Aitken mode in mass mixing ratio per timestep. This slope is calculated to be 2.3×10^9. For 1 ppbv of SO_2, with the same OH concentration, this gives a transfer timescale of around 1.7 days.

3.1.4 Sulphate aerosol size distribution

The Aitken and accumulation mode are described using log-normal size distributions of the number, which require two parameters, a modal radius and a distribution width. Parameters used in HadGEM1 and those introduced for HadGEM2 are shown in Table 1. In HadGEM1, the Aitken mode was associated with a large modal radius that is not supported by observations. This has been changed for HadGEM2, using the smallest log-normal distribution of urban environment aerosols parameterised by Janicke [1993] for the Aitken mode.

3.1.5 Effect on cloud droplet size

In both HadGEM1 and HadGEM2, sulphate aerosols influence the number and size of cloud droplets. The latter is diagnosed using the effective radius (r_e) of the cloud

	Aitken mode		Accumulation mode	
Model	r_0	σ	r_0	σ
HadGEM1	0.024	1.45	0.095	1.40
HadGEM2	0.0065	1.30	0.095	1.40

Table 1: Parameters of the log-normal size distributions describing the Aitken and accumulation-mode sulphate aerosols. r_0 is the modal radius (μm), σ is the geometric standard deviation.

droplet size spectrum; r_e is also retrieved from satellite observations, thus providing a mean of assessing model performance (see section 6.4.4). The effective radius is determined by the amount of cloud water and the number of cloud droplets. Calculating the latter involves a conversion from aerosol mass to aerosol number concentration, which requires the size distribution of the aerosol to be specified. In HadGEM1, this conversion involves two inconsistencies. Firstly, the *total* sulphate mass is used, whereas only those modes which interact with cloud (the accumulation and dissolved mode) should be used. Secondly, the parameters of the size distributions are different to those assumed in the rest of the model. Those inconsistencies are now removed from HadGEM2. These changes are generalised to all aerosol species that act as cloud condensation nuclei.

3.1.6 Impact of changes to the sulphur cycle scheme

Several model simulations have been performed to diagnose the impact of the changes to the sulphur cycle scheme and the radiation fields. Table 2 summarises these experiments and their results, compared against those from the standard HadGAM1 configuration.

The impact of the new rainout scheme, including re-evaporation to the accumulation mode, is assessed comparing experiments CONTROL and RAIN. The proportion of sulphate in the accumulation-mode increases from 22% in HadGAM1 to 39%. The sulphate lifetime has increased by almost a day, reaching 54 hours. The total sulphate burden changes by only 15% but, as the accumulation-mode sulphate is optically more efficient, this translates into a near doubling of the aerosol optical depth and a direct radiative forcing more negative by 17%. With the addition of mode-merging and the improvement to the ammonium sulphate deposition (experiment RAIN+COND), the proportion of accumulation-mode sulphate increases further to 61% while the total sulphate burden only increases by 6% compared to its value in HadGEM1. As expected for more accumulation-mode sulphate, its optical depth and direct perturbation both increase in magnitude, by 142% and 40%, respectively. The lifetime almost reaches 3 days, a value compatible with results for other models [Barrie *et al.* 2001]. When the revised Aitken mode size distribution is used (experiment RAIN+COND+SIZE), the fraction of accumulation mode represents 75% of the total mass with a reduction of the sulphate burden to 2.75 mg m^{-2}. Those two effects compensate and the aerosol optical depth and the direct radiative forcing do not change significantly. Finally, when the cloud droplet number calculation is made consistent with the other changes (experiment ALL), the aerosol mass interacting with clouds is now smaller. This decreases the wet deposition of sulphate and slightly increases the

Experiment	Description
CONTROL	Standard HadGAM1
RAIN	Includes new aerosol rainout
RAIN+COND	Also includes the revised sulphate condensation and mode-merging
RAIN+COND+SIZE	Also includes the revised Aitken sulphate size distribution
ALL	Also includes the revised cloud droplet number calculation

Experiment	$S_{\rm acc}/S_{\rm tot}$	AOD	DRF ($\rm Wm^{-2}$)	Burden ($\rm mg\ m^{-2}$)	τ (hours)	$r_{\rm e}$ (μm)	TOA ΔF ($\rm Wm^{-2}$)
CONTROL	0.22	0.007	−0.45	3.01	27.1	9.7	
RAIN	0.39	0.013	−0.53	3.46	53.9	9.4	
RAIN+COND	0.61	0.017	−0.63	3.18	69.2	9.5	
RAIN+COND+SIZE	0.75	0.017	−0.63	2.75	70.9	10.5	+1.75
ALL	0.75	0.018	−0.67	2.86		11.6	+3.74

Table 2: Description of and results from standard and modified HadGAM1 simulations. Shown are the ratio of accumulation-mode sulphate to total sulphate ($S_{\rm acc}/S_{\rm tot}$), sulphate aerosol optical depth at 0.55 μm (AOD), aerosol direct radiative forcing (DRF), total sulphate burden, loss lifetime of combined accumulation and dissolved mode sulphate (τ), effective cloud droplet radius ($r_{\rm e}$), and top of the atmosphere net radiation (TOA ΔF).

burden, with small consequences on the aerosol optical depth and direct perturbation. As the in-cloud aerosol mass is smaller, the droplet number decreases, therefore increasing the cloud droplet effective radius to 11.6 μm. As fewer, larger droplets are less reflective than more, smaller droplets, the atmosphere appears darker and the top-of-atmosphere net downward radiation increases by 2 $\rm Wm^{-2}$.

A schematic flow diagram of the sulphur cycle is presented in Figure 5. Burden and mass flux values are given for experiments CONTROL, RAIN, and RAIN+COND as listed in Table 2. (Note that burdens and fluxes are given in term of *sulphur* mass, not *sulphate* mass as in the table). The most significant changes happen to the sulphate masses and mass fluxes. Dimethylsulfide (DMS) and sulphur dioxide do not change significantly. As expected, the changes made to the sulphur cycle have increased the burden in the accumulation mode and decreased it in the Aitken mode. The revision of the dry oxidation by OH and the added mass transfer through mode-merging from Aitken sulphate and re-evaporation from dissolved sulphate explain this new behaviour. As the accumulation burden is larger, the associated dry and wet depositions of this mode increase and the depositions of Aitken sulphate decrease.

3.2 Biomass-burning aerosol

3.2.1 Introduction

The biomass-burning aerosol scheme was included for the first time in HadGEM1. This scheme is described in Davison *et al.* [2004]. It is a modal scheme, where the

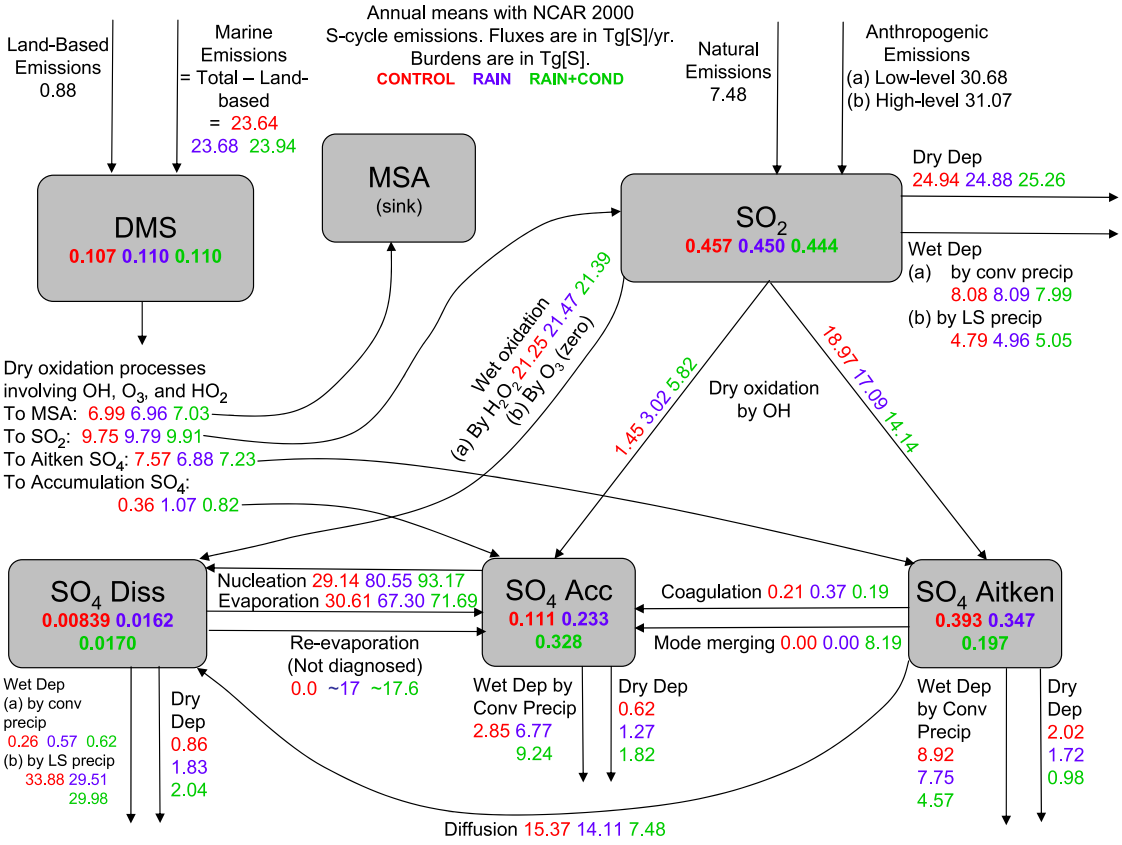

Figure 5: Flow diagram of the sulphur cycle scheme showing annual mean mass fluxes (arrows, in Tg[S] yr^{-1}) and burdens (boxes, in Tg[S]) for HadGEM1 (red), including the new rainout (purple), and with revised condensation and added mode-merging (green).

biomass-burning aerosol mass is partitioned into three modes. The first one represents the freshly emitted aerosol. The aerosol ages after an e-folding time of 1 day into a second mode, called aged mode. The third mode represents the biomass-burning aerosol mass that is dissolved into cloud droplets, thus allowing the aerosol to exert indirect effects. Deficiencies in the HadGEM1 biomass-burning scheme are:

- Size distribution and absorbing properties do not match observations;
- The aerosol is not represented as being hygroscopic, which is inconsistent with it exerting indirect effects;
- The aerosol ageing is slow compared to observations and does not account for condensation of other chemical species;
- The emission dataset is not described by any citable reference.

Here, we review the changes that were made to address those points.

3.2.2 Size distribution and absorption

Haywood *et al.* [2003] describes measurements made by the Met Office aircraft during the field campaign SAFARI 2000. This campaign targeted the biomass-burning aerosol in southern Africa. Flying in the aged regional haze plume, they find a multimodal size distribution. The accumulation mode size can be described using a mode radius of 0.12 μm with a geometric standard deviation of 1.3. This contrast with the values used for the aged mode in HadGEM1, where the mode radius and standard deviation are both significantly larger, at 0.2 μm and 1.58 respectively. Figure 6 shows the HadGEM1 size distribution compared to that measured by the aircraft (multimodal) and a log-normal fit of the measured accumulation mode. In order to correctly represent the extinction, the model should use a size distribution closely matching that from the aircraft for particle radii between 0.09 and 0.3 μm. As both the mode radius and the width of the distribution used in HadGEM1 are too large, especially for the aged mode, HadGEM1 size distributions differ from the observed distributions. In HadGEM2, a fit of the aircraft size distribution is used and obviously improves the comparison significantly.

According to aircraft measurements, biomass-burning aerosols are moderately absorbing, with a single-scattering albedo of 0.91 $\pm$ 0.4 at 0.55 μm. In HadGEM1, the single-scattering albedo for aged biomass-burning is 0.80, thus overestimating the absorption by a factor of two. This large absorption stems from the assumed chemical composition of the biomass-burning aerosol. It is assumed that 10% of the mass is black carbon, a strongly absorbing aerosol. Reducing that fraction according to observations helps increase the single-scattering albedo (*i.e.* decrease the absorption). Table 3 summarises the changes made to the biomass-burning optical properties in HadGEM2 from their values in HadGEM1. Note that the biomass-burning aerosol density was also updated.

3.2.3 Hygroscopic growth

Although biomass-burning aerosols are considered as cloud condensation nuclei, they are not modelled as experiencing hygroscopic growth. This is inconsistent. Hygro-

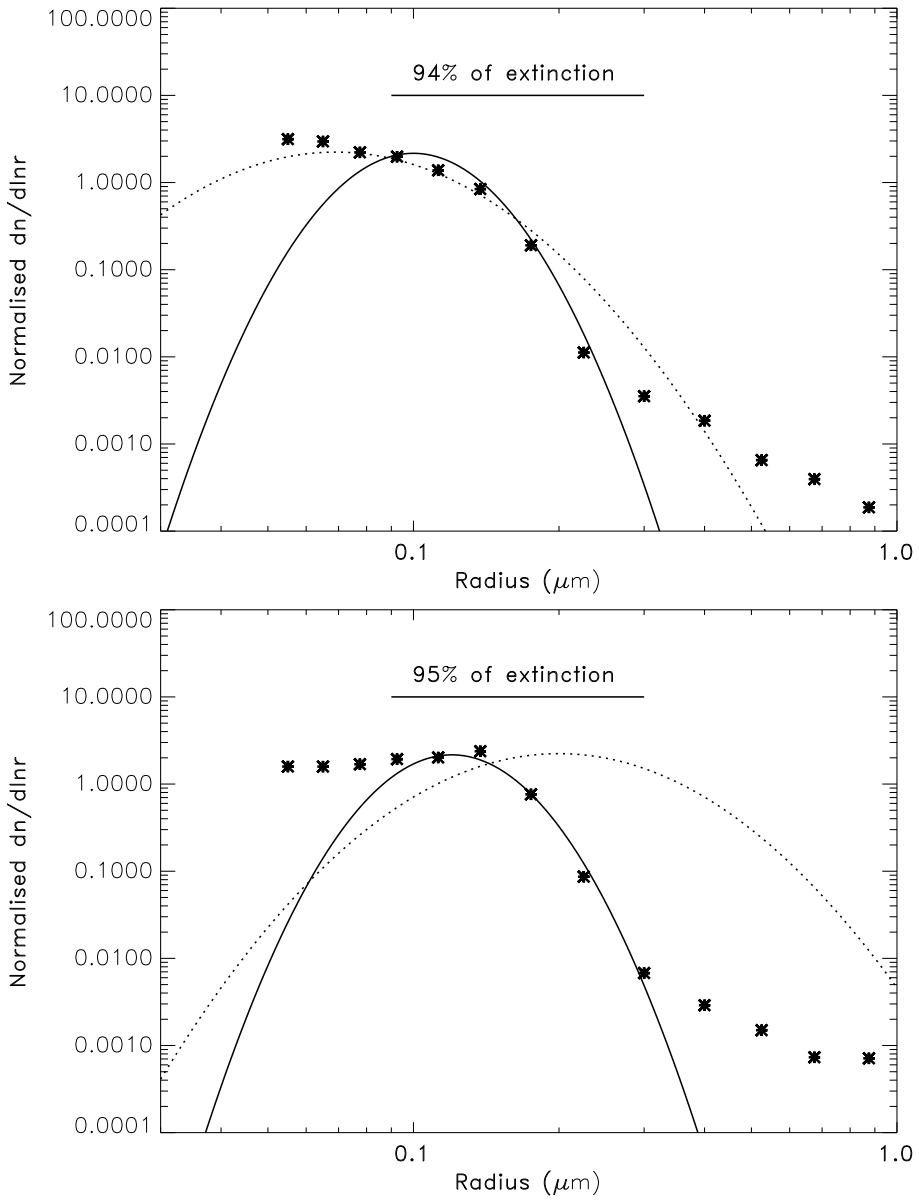

Figure 6: Size distribution for fresh (top) and aged (bottom) biomass-burning aerosol using the HadGEM1 parameters (dotted lines), revised parameters introduced for HadGEM2 (solid line), and as observed from *in situ* aircraft measurements during SAFARI 2000 (points).

Quantity	HadGEM1	HadGEM2
r_0 – fresh	0.069	0.100
r_0 – aged	0.200	0.120
σ – fresh	1.65	1.30
σ – aged	1.58	1.30
f_{BC} – fresh	10%	8.75%
f_{BC} – aged	10%	5.40%
ρ	1500	1350

Table 3: Properties of the fresh and aged biomass-burning aerosols as used in HadGEM1 and revised for HadGEM2. Aerosol properties listed are: modal radius (r_0 in μm), geometrical standard deviation (σ), mass-fraction of black carbon (f_{BC}) and density (ρ in kg m^{-3}).

scopic growth is therefore introduced following observations made during SAFARI 2000 [Magi and Hobbs 2003]. As the result, the specific extinction coefficient for biomass-burning aerosols increases by a factor of 20 between the dry and fully hydrated aerosol, as shown on Figure 1.

3.2.4 Ageing

The e-folding timescale for biomass-burning aerosol ageing is 24 hours in HadGEM1. Field observations from SAFARI 2000 suggest a much quicker ageing [Abel *et al.* 2003]. Based on these observations, the ageing timescale is therefore reduced to 6 hours. This enhances further the importance of the aged mode, which now holds most of the total biomass-burning aerosol mass. The increase in the rate of ageing also make the transformation of biomass-burning aerosols into cloud condensation nuclei more efficient. As aerosols dissolved in cloud droplets are more susceptible to removal from the atmosphere because of rainout, an increase in the wet deposition can be expected. However, this tendency is counteracted by the application of the revised aerosol rainout scheme (described in section 3.1.2) to the biomass-burning aerosols. With the rainout, the aged mode is replenished by the mass of re-evaporated dissolved aerosol.

Observations also show that ageing is caused by a variety of processes. These include aerosol coagulation and changes in physical structure. Using different size distributions and fractions of black carbon (hence different absorbing properties) for the fresh and aged mode, as described in the previous section, accounts for those processes to a certain extent. However, volatile organic compounds (VOCs) also condense onto the aerosols as part of the ageing process. It is beyond the capacity of an aerosol scheme to attempt to simulate such a process in detail, but a simple approach was adopted, whereby the mass of biomass-burning aerosols upon ageing in increased by approximately 1.62. This is the ratio of the black carbon mass-fraction in fresh (8.75%) and aged (5.4%) aerosols. This ratio therefore accounts consistently for the decrease in the fraction of black carbon in biomass-burning aerosols upon ageing, and is also consistent with the findings of Abel *et al.* [2003].

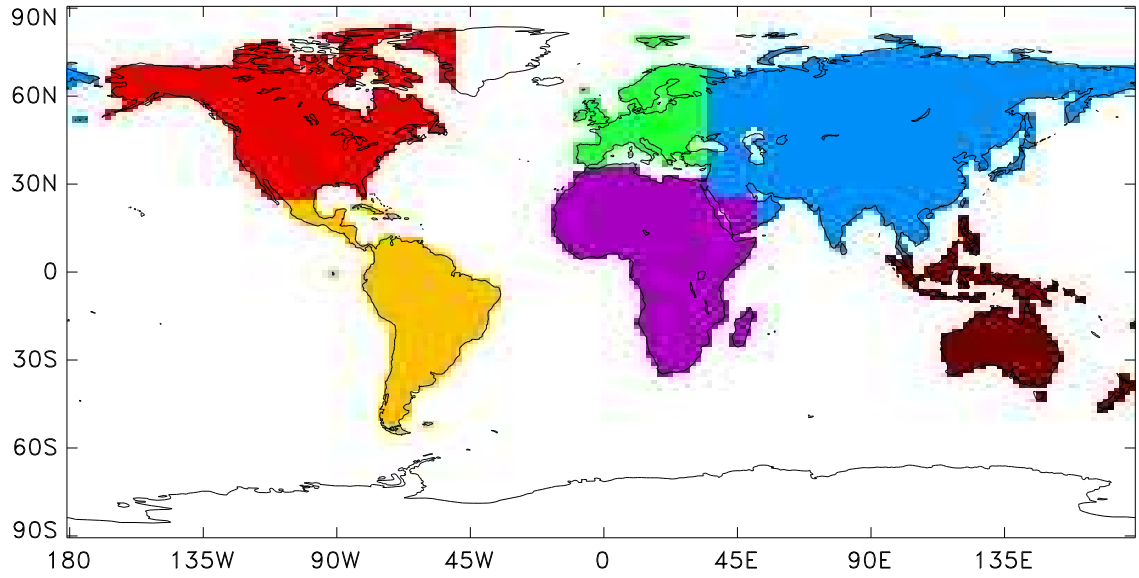

Figure 7: Geographic regions used in determining the temporal evolution of biomass-burning emissions.

3.2.5 Emission dataset

Biomass-burning emissions to the fresh mode used in HadGEM1 are based on a historical dataset which has no clear provenance and is not readily "referenceable". Newer datasets were developed recently for use in climate modelling and those include biomass-burning aerosol emissions [Dentener *et al.* 2006] for the years 1750 and 2000, at monthly-mean resolution. Unfortunately, the temporal evolution between those two years is not given. Therefore, assumptions had to be made (similar assumptions were made when creating the standard HadGEM1 emission datasets). Following advice from those scientists who created the dataset, changes in regional population were used to approximate the time-profile of biomass-burning emissions. Population statistics taken every fifty years from 1750 to 2000 for six geographical regions were used [United Nations 1999]. The regions for which population data were defined were given as Africa, Asia, Europe, Latin America and the Carribean, Northern America, and Oceania. Those regions are shown in Figure 7. Certain infelicities in the mask (*e.g.* Greenland and the Arabian peninsula) are not important as there is little or no biomass-burning in these regions. For each region, the time-profile of biomass-burning changes from 1750 to 2000 was scaled to follow the changes in population. The resulting time-evolution of the emissions, compared to that used in HadGEM1, is shown in Figure 8. It is worth noting that the changes from pre-industrial times are less in the new emission dataset than in the dataset used in HadGEM1. It will have implications on the magnitude on the radiative perturbation by biomass-burning aerosols.

3.2.6 Impact of changes to the biomass-burning aerosol

Changes made to the biomass-burning aerosol representation are such that significant changes to the radiative perturbation can be anticipated. The changes to the

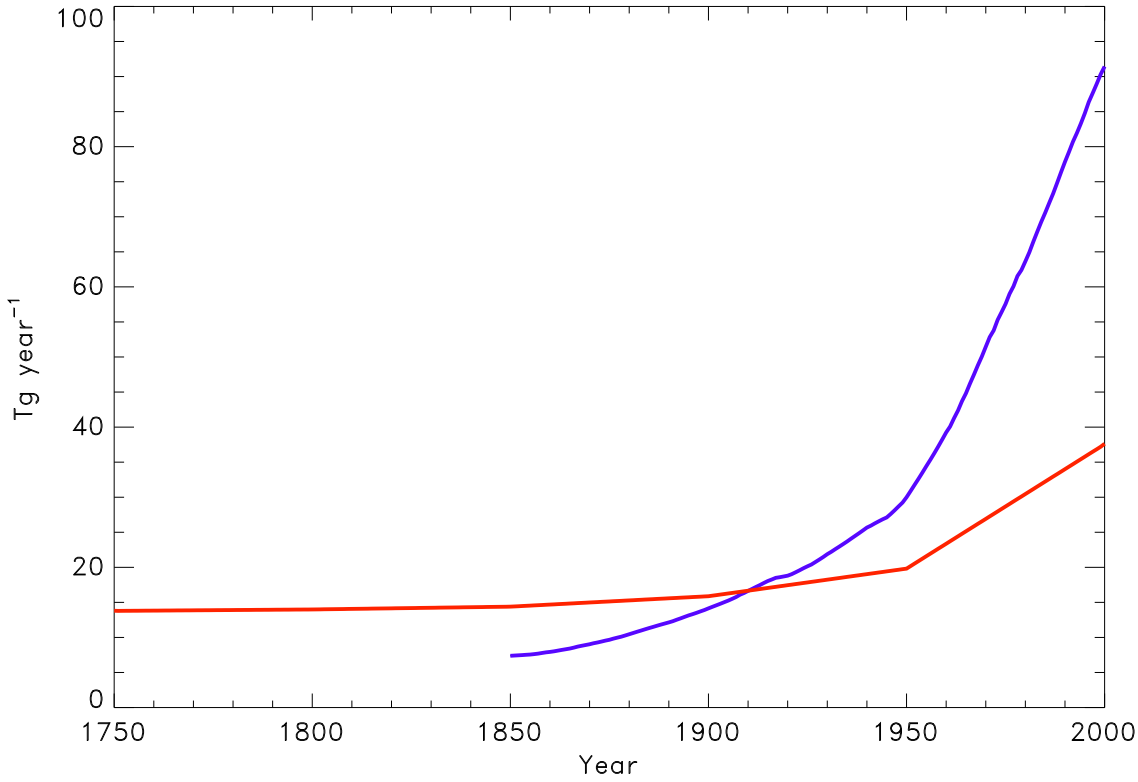

Figure 8: Time evolution of biomass-burning emissions as used in HadGEM1 (blue line) and as introduced for HadGEM2 (red line).

optical properties will impact upon the direct effect, the changes to the particle size distributions upon the indirect effect, and the changes to the emissions upon both of these.

Figure 9 show the annual-mean direct perturbation caused by changes in biomass-burning aerosol loading between 1860 and 2000 for HadGEM1 and using the revised scheme designed for HadGEM2. The first and most obvious change is that the annual-mean direct perturbation has changed from being positive (warming) to negative (cooling). This is a consequence of changes in absorbing properties. As the revised single-scattering albedo is larger, the critical single-scattering albedo threshold is reached less often and the biomass-burning direct radiative perturbation is seldom positive. Regions with large positive perturbations in HadGEM1 are now associated with negative perturbations (*e.g.* Sahara) or slightly positive ones (*e.g.* stratocumulus region off the coast of Namibia). In boreal regions of Canada and Russia, positive perturbations now appear in HadGEM2. They are due to a decrease in biomass-burning emissions since pre-industrial times.

Unlike the direct effect, it is not possible to unambiguously determine the radiative perturbation due to the indirect effects of biomass-burning aerosols. This is because of the non-linear nature of the indirect effects, which means that the choice of background aerosol assumed affects the estimate of the perturbation. In other words, trying to quantify the indirect effect of biomass-burning aerosols using pre-industrial levels of sulphate aerosols would yield different results to using present-day levels.

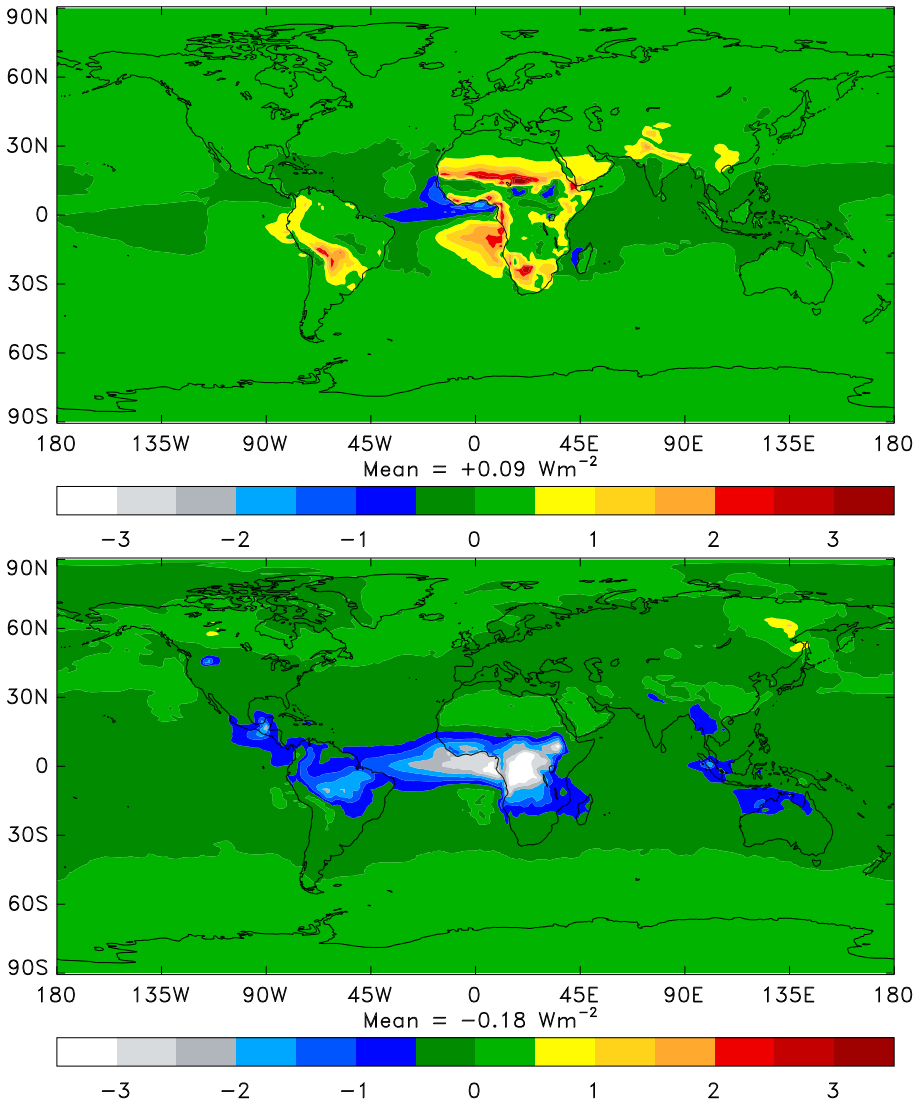

Figure 9: Annual-mean direct forcing by 1860–2000 changes in biomass-burning emissions in HadGAM1 (top) and as revised for HadGAM2 (bottom).

Sulphate, biomass-burning, and other aerosol emissions have evolved together over the industrial period, and one can only determine their combined indirect effects. However, it is possible to determine the effect on this combined effect of the changes made to the biomass-burning aerosol scheme. Figure 10 shows the annual-mean indirect perturbation caused by changes in all simulated aerosols between 1860 and 2000. The top panel includes the updated sulphate aerosol scheme (see section 3.1) and the HadGEM1 biomass-burning scheme. The bottom panel shows the impact made on that distribution when using the revised biomass-burning scheme. The indirect perturbation is stronger where stratiform water cloud cover is extensive, such as the sub-tropical stratocumulus areas. The nature of the indirect effect makes its distribution quite noisy: it is obtained using two parallel model runs that evolved differently (*i.e.* had different "weather"). These different evolutions also mean that not all changes may be attributed to changes in biomass-burning modelling. The global-average estimate of the indirect perturbation is therefore associated with a measure of the statistical noise generated by this approach. This uncertainty range is larger than the mean change between the two simulations, which means that the results ought to be treated in a rather qualitative manner, as the statistical significance is not well established. The revised biomass-burning scheme reduces the magnitude of the negative indirect perturbation. This is partly explained by the change in emission dataset, the new one showing a much less pronounced increase during the industrial period and also being higher in the pre-industrial period. Changes in the size distribution, ageing processes and aerosol rainout also produce more aerosol able to act as cloud condensation nuclei. This increases the background (pre-industrial) concentration of cloud droplets in the revised simulation, making the clouds less susceptible to further anthropogenic change.

In summary, changes made to the biomass-burning scheme make the direct perturbation more negative and the indirect perturbation less negative. Overall, the negative perturbation is increased by 10 to 15%.

3.3 Black carbon and sea salt aerosols

Both black carbon and sea salt aerosol representations were kept mostly unchanged from what they are in HadGEM1. They are included here for the sake of completeness. The black carbon scheme closely resembles that of biomass-burning aerosols. It is described in Roberts and Jones [2004]. Changes made to the rainout apply to the wet deposition of the aged mode. Sea salt aerosol is fully diagnostic. Its number concentration is computed at each timestep depending on near-surface wind speed, and is not transported or deposited [Jones *et al.* 2001]. When interacting with radiation, sea salt modelling accounts for hygroscopic growth, as shown on Figure 1. No changes have been made to the sea salt representation.

4 New aerosol species

On top of the improvements made to existing aerosol species described in the previous section, two new aerosol species that were not included in HadGEM1 are now introduced for HadGEM2. These are the secondary organic and mineral dust aerosols.

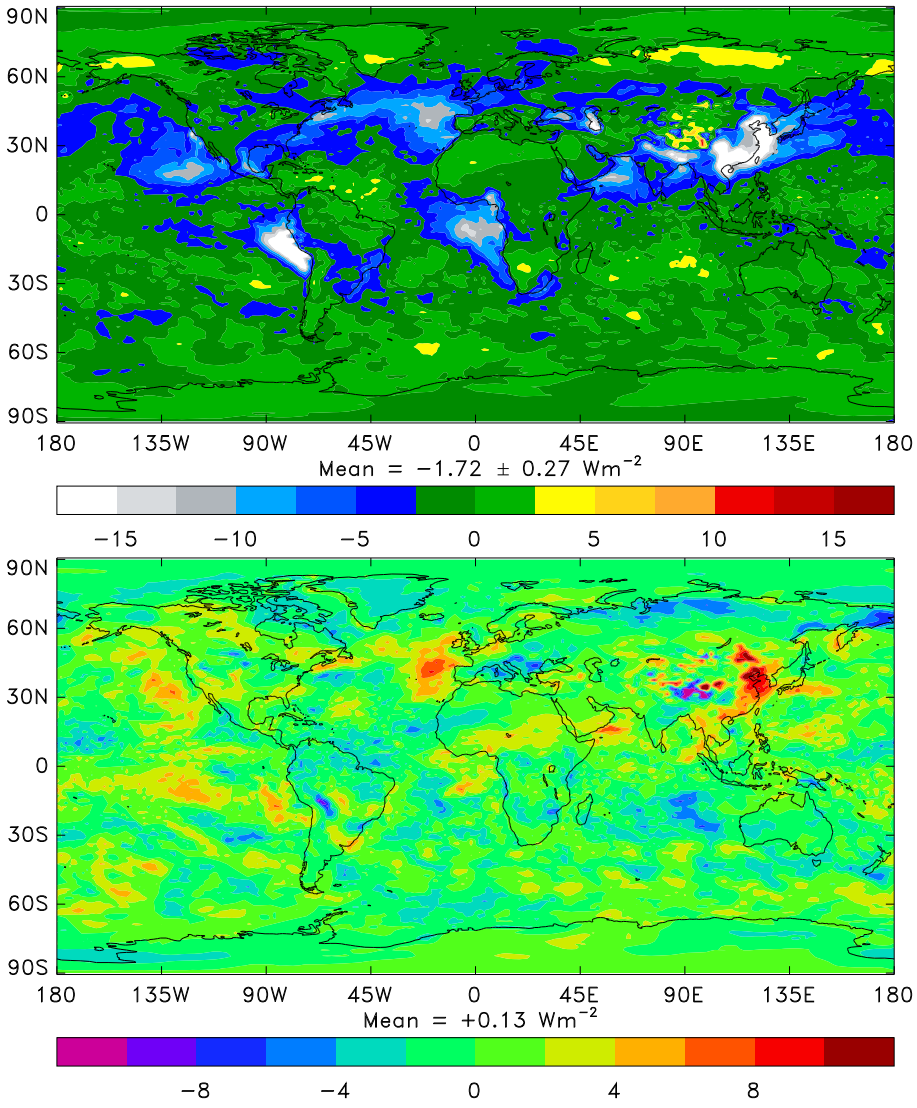

Figure 10: Top panel: annual-mean indirect forcing by 1860–2000 changes in all aerosols, using the standard HadGEM1 biomass-burning aerosol scheme. Bottom panel: Impact on the forcing shown on top panel of using the revised biomass-burning aerosol scheme. Positive values indicate areas where the forcing has decreased in magnitude.

4.1 Secondary organic aerosol

The secondary organic aerosol is the product of the oxidation of biogenic volatile organic coumpounds such as terpenes emitted by vegetation (*e.g.* Cahill *et al.* [2006] and references therein). This is a natural aerosol, mostly observed in forested regions. Its addition is therefore useful in order to represent the aerosol loading observed where none of the species included in HadGEM1 is significantly present (typically, continental areas far from human sources, such as central Russia). In HadGEM2, the secondary organic aerosol is introduced as a simple climatology of monthly-averaged fields, obtained using the terpene oxidation modelling of the STOCHEM chemistry transport model [Derwent *et al.* 2003]. On a global and annual mean, the burden of secondary organic aerosols is 2.2 mg m^{-2}.

Ground-based observations provide the secondary organic aerosol optical properties. Size distributions are derived from ground-based sun-photometer measurements at three Russian cities (Yekaterinburg, Tomsk, and Krasnoyarsk). Those sites are part of the wider AERONET network described in section 6.2. Although those are major cities, they are believed to exhibit a significant contribution of secondary organic aerosol in summer months from nearby forests. The secondary organic aerosol size distribution is also expected to be similar to that of anthropogenic industrial aerosols. A single log-normally distributed aerosol size distribution is assumed, with a mode radius of 0.095 μm and a geometric standard deviation of 1.5. The complex refractive index is taken to be wavelength-independent, from extrapolating results published in Lund-Myhre and Nielsen [2004], and was assumed to be non-absorbing throughout the majority of the solar spectrum, much like that of ammonium sulphate. The density is assumed to be 1050 kg m^{-3} [Bahreini *et al.* 2005], leading to a specific extinction coefficient of 6.23 m^2 g^{-1} at 0.55 μm when calculated using a Mie scattering code. Hygroscopic growth is modelled using mean growth factors determined experimentally by Varutbangkul *et al.* [2006] which are derived for a range of organic substances. These growth factors are in reasonable agreement with those determined from atmospheric measurements by Chan and Chan [2003].

Secondary organic aerosols exert both direct and indirect radiative perturbations. Being a natural aerosol, it increases both the present-day and pre-industrial aerosol loading. The latter means this aerosol acts to reduce the indirect radiative perturbation, as pre-industrial clouds now include another contribution to the cloud droplet size calculation.

4.2 Mineral dust

The mineral dust scheme for HadGAM2 is based on the dust model which had been developed for use with HadAM3, the model that precedes HadGAM1. It includes code for an emission scheme, deposition through gravitational settling, turbulent mixing and below-cloud scavenging and the direct radiative effects of dust [Woodward 2001]. Unlike other aerosol species that rely on emission datasets, dust production is calculated interactively from climate model fields at every timestep. As dust uplift is very sensitive to local climatic conditions (in reality as well in models) dust schemes need to be tuned to the model in which they are imbedded. At the time of writing the HadGEM2 model has not been finalised and the dust scheme is still undergoing

tuning. Dust results presented in this note therefore correspond to developmental versions of the scheme.

The mineral dust scheme is based on that described in Woodward [2001] and includes the following changes:

- Dry threshold friction velocity is obtained from the work of Iversen and White [1982];
- The horizontal flux is calculated for a size range from 0.0316 to 1000 μm radius. This is divided into 9 bins, the 6 smallest as in Woodward [2001]; the 3 larger bins have boundaries at 31.6, 100, 316 and 1000 μm. The parent soil size distribution for the 3 new bins is obtained from the sand fraction, assuming $\frac{\mathrm{d(Mass)}}{\mathrm{d(log(radius))}}$ is constant over this range. A normalisation factor of 5.22 is used in the horizontal flux equation, instead of the 2.61 in Woodward [2001];
- Total vertical flux is obtained from total horizontal flux, using equation (1) from Woodward [2001]. (Note that the RHS of this equation should include a factor of 0.01, if SI units are used). The total flux is then partitioned across the smallest 6 size bins, in proportion to the parent soil mass size distribution. Clay fractions greater than 20% are reset to 20% here, in order to avoid excessive dust production at a few points.
- Dust emissions are suppressed on steep slopes (half peak to trough height greater than 150 m) to avoid anomalous dust production due to a wind speed oscillation problem in the developmental version of HadGEM2.

5 Overall impact and comparison against other climate models

In HadGEM1, aerosols exert a direct perturbation with respect to pre-industrial conditions of $+0.18$ Wm^{-2} and a total (direct plus indirect) perturbation of -1.01 Wm^{-2}. When the above changes are included and the model is configured to emulate the final setup of HadGEM2, the direct and total perturbations become -0.13 Wm^{-2} and -1.22 Wm^{-2}. The overall effect of improvements made to the aerosol simulation is therefore to switch the direct forcing from a warming to a cooling contribution, and increase the total perturbation by 21%. The change in the sign of the direct forcing is due to an enhanced contribution by sulphate aerosols (the sulphate forcing doubles from -0.14 Wm^{-2} in HadGEM1 to -0.33 Wm^{-2} in HadGEM2) and to a negative contribution by the less absorbing biomass-burning aerosols. Changes in the total perturbation also include changes in indirect effects, which are limited by the introduction of the natural secondary organic aerosol and higher pre-industrial biomass-burning levels. Both act on pre-industrial and present-day clouds and reduce the possible range of action on cloud droplet size.

Table 4 lists the component aerosol burden and optical depths as simulated in a prototype of HadGEM2. The total aerosol burden is 79 mg m^{-2}. The associated aerosol optical depth is 0.109 at 0.55 μm. Also shown in Table 4 are the results of an

Aerosol species	Burden		Optical depth	
	HadGEM2	AeroCom	HadGEM2	AeroCom
Sulphate [SO_4]	3.95	3.9 (1.8–5.3)	0.022	0.034 (0.015–0.051)
Black Carbon	0.74	0.39 (0.22–1.00)	0.004	0.004 (0.002–0.009)
Biomass-burning	2.50	–	0.018	–
POM	–	3.3 (0.9–5.0)	–	0.019 (0.006–0.030)
Sea salt	49.16	12.6 (4.8–25.8)	0.052	0.030 (0.020–0.054)
Mineral dust	20.50	39.1 (8.8–57.8)	0.005	0.032 (0.012–0.053)
Secondary organic	2.16	–	0.008	–
Total	79.01	56 (34–92)	0.109	0.127 (0.065–0.151)

Table 4: Component and total aerosol burdens (mg m^{-2}) and optical depths (at 0.55 μm) for present-day emissions, as simulated by HadGEM2 and summarised for the models participating in the AeroCom project [Kinne *et al.* 2006]. AeroCom results are the median of all participating models, with the smallest and largest estimates given in brackets. POM stands for particulate organic matter.

aerosol modelling inter-comparison initiative, AeroCom. Nine chemistry transport or general circulation models were run using their own or prescribed emission datasets, the latter being described in Dentener *et al.* [2006]. Kinne *et al.* [2006] compares the distributions and global averages of the aerosol optical depth and provide the figures shown in Table 4 (median, minimum and maximum estimates). Ranges are large, showing that aerosol modelling is still largely uncertain. Kinne *et al.* [2006] conclude that although the models agree reasonably well on the annual, global average of the total aerosol optical depth, there are still significant differences among models at regional levels. There is also a persistent trend for models to underestimate the aerosol optical depth compared to satellite observations. AeroCom models do not simulate the biomass-burning aerosol in itself, but rather discriminate its black carbon and particulate organic matter (POM) components. For this reason, it makes more sense to compare the sum of black carbon and biomass-burning in HadGEM2 (burden of 3.24 mg m^{-2}, optical depth of 0.022) against the sum of black carbon and POM from AeroCom (burden of 3.69 mg m^{-2}, optical depth of 0.023). AeroCom does not include secondary organic aerosols. Excluding sea salt, HadGEM2 burdens do not show significant under- or overestimations. Due to assumptions in its modelling, sea salt is associated with a large burden but, as most of the mass lies in the coarser mode, this does not translate into an overestimated optical depth. For all available species except mineral dust, aerosol optical depths in HadGEM2 are within the range obtained by AeroCom models. As stated in section 4.2, the version of the dust scheme used in this note is not final, and is expected to improve before HadGEM2 is finalised. For the moment, the mineral dust burden is at the lower end of the AeroCom range, which may explain the underestimated optical depths.

Schulz *et al.* [2006] focus on the direct forcing with respect to pre-industrial conditions from AeroCom models. They report a global, annual average for the all-sky forcing of -0.22 ± 0.16 Wm^{-2} with individual model estimates ranging from $+0.04$ to -0.41 Wm^{-2}. The standard deviation measuring the model diversity is ± 0.16 Wm^{-2}. In that respect, it must be noted that the large positive forcing simulated in

HadGEM1 would have been an outlier within the AeroCom models. Although it can be argued that no AeroCom model holds the "true" aerosol forcing, the consensus is that the present-day aerosol direct radiative effect is negative. HadGEM1 has therefore an expected behaviour which is fortunately corrected in HadGEM2. The direct forcing of -0.13 Wm^{-2} simulated by the latter is well within the AeroCom range. The indirect effects are much more uncertain and are not directly considered in AeroCom. Penner *et al.* [2006] uses three global models and shows that the total aerosol radiative perturbation ranges from -0.4 to -1.4 Wm^{-2} among them. HadGEM2 is at the higher end of that range but it is difficult to assess whether its indirect effects are overestimated or not.

6 Comparison against observations

There are now a wide range of dedicated observations that have been used to validate several aspects of aerosol representations in numerical models (e.g. Reddy *et al.* [2005], Liu *et al.* [2006], Ginoux *et al.* [2006]). Observations provide speciated chemical concentrations, or optical parameters such as the aerosol optical depth, single-scattering albedo. Some aspects of cloud microphysics are also observed.

6.1 Sulphate aerosol mass concentrations

Surface sites of the EMEP and IMPROVE measurement networks and those of the University of Miami measure the sulphate aerosol mass concentration. A dataset for comparison against modelled fields has been compiled by Stier *et al.* [2005]. Figure 11 shows such a comparison for HadGEM1 and HadGEM2. There is no clear change between the two models. The slope of the fitting line is closer to 1 in HadGEM2, but the correlation decreases slightly. From the point of view of sulphate burden, the improved sulphate scheme may not be significantly better than the old one, but it is certainly not worse. It must also be stressed that the main improvement to the sulphate scheme was in the partioning of the total sulphate mass between the modes. The total burden has always been reasonable.

6.2 Ground-based sun-photometers

The Aerosol Robotic Network (AERONET) gathers data from about 300 automated sun-photometers worldwide. AERONET measurement and retrieval techniques, as well as results for key aerosol types, are described in Dubovik *et al.* [2002] and references therein. By pointing directly at the sun and measuring the atmospheric transmission, they provide a direct measurement of the aerosol optical depth at varying wavelengths, with all instruments equipped with a filter at 0.44 μm. Inversion algorithms, based on measurements of the angular dependence of the extinction, also provide the single-scattering albedo, albeit conditions for a successful retrieval are more stringent than for the optical depth and the uncertainty in the retrieved value is larger. These *in-situ* measurements allow a very good sampling of the day-to-day variability of the aerosol loading and absorbing properties, although cloudy skies must be screened out. Quality-assured algorithms provide retrievals that can be used with

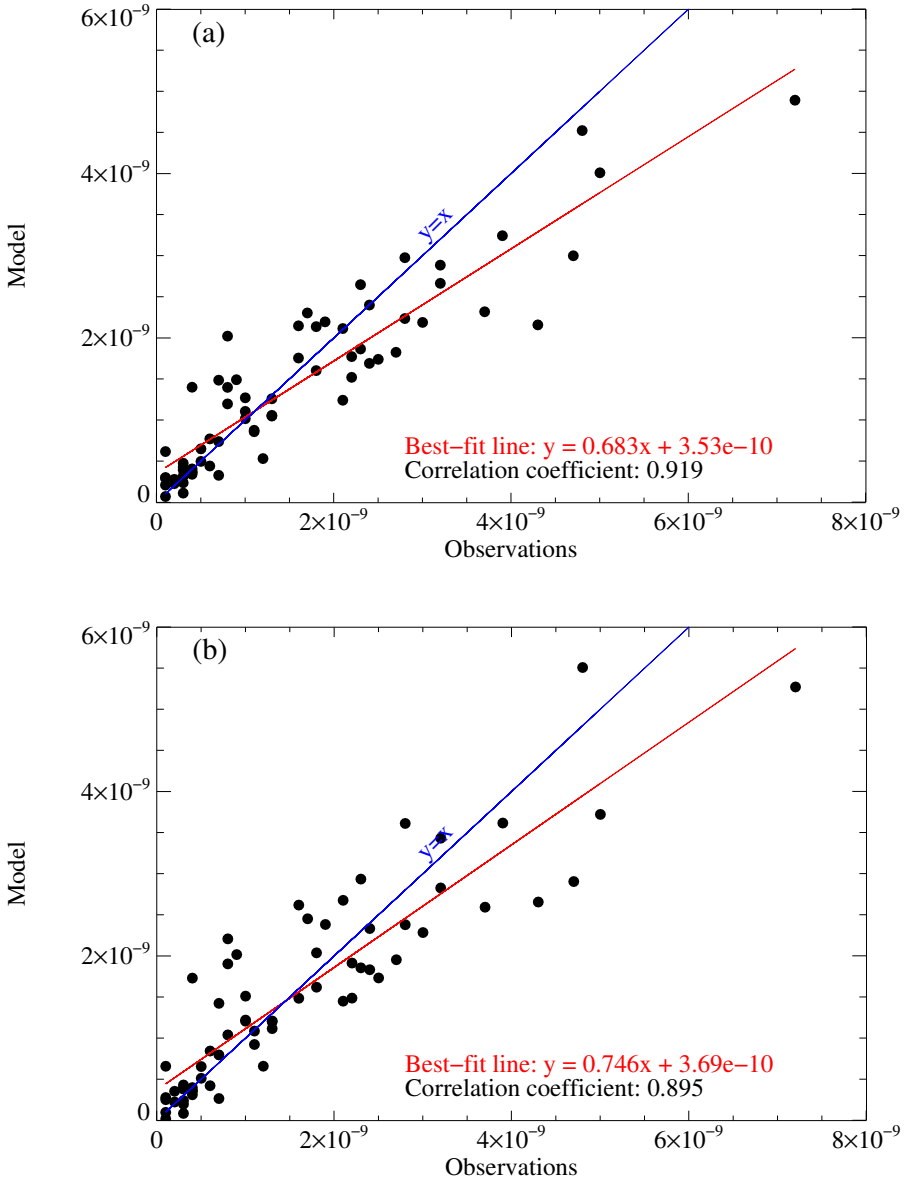

Figure 11: Annual average of sulphate aerosol mass ($kg[SO_4]m^{-3}$) as modelled in HadGEM1 (a) and HadGEM2 (b) compared to observations from EMEP, IMPROVE, and University of Miami networks.

high confidence. The instruments have been strategically placed around the world and the main aerosol types are observed. Some of those sites have been monitoring aerosol properties for a decade and allow the removing of the inter-annual variability and isolation of the climatological signal. In the following, we use sites where all monthly means were made from at least 10 daily averages and for at least two years.

6.2.1 Aerosol optical depth

Figure 12 shows the modelled seasonal distributions in HadGEM2 with seasonal means from AERONET overlaid. The model distributions are from a 10-year run using transient emissions for the 1990s. The squares representing the AERONET sites follow the same colour scale as the global distribution. Here, the aerosol optical depth is given at 0.44 μm. Some locations are doing particularly well while others exhibit a poor match of observed averages. The model does quite well over North America. The east-west decrease in optical depth is well reproduced, with an impressive model performance in the summer, although optical depths on the east coast in autumn and winter seem to be under-estimated. The large optical depths observed at Mexico City are not matched by the model. This is a very polluted location, and a global model grid-box is not expected to match those local maxima. In South America, agreement is reasonable, except over Amazonia in winter and spring. In Europe, although the observed climatology for the Mediterranean basin is well reproduced, western Europe is associated with significantly under-estimated optical depths throughout the year, especially in winter months. Over India, China, and Japan, the models does well, especially when simulating the strong gradient over China. Over Africa, while the situation is good in southern Africa, the under-estimated optical depths in the northwest is obvious. The same happens in the Middle East, for some months.

The two areas and periods where the model does poorly are western Europe in winter and northwestern Africa throughout the year. For Europe, the underestimation stems from the chemistry included in the sulphur cycle, and missing species. Sulphur dioxide is oxidised into sulphate, which eventually becomes ammonium sulphate aerosols, by hydrogen peroxide and ozone. Only the former oxidation path is currently enabled in HadGEM2. As production of hydrogen peroxide is limited by the available amount of sunlight, it is much less efficient during the winter season. Ozone does not have such a limitation but requires assumptions in its modelling. Although there is provision for future inclusion of the ozone oxidation path in the model, it is not currently used, thus limiting production of sulphate aerosols during winter. The model does also not include nitrate aerosols. Met Office aircraft observations made around the United Kindgom have shown that nitrate can be as abundant as sulphate in that area. Adding a nitrate aerosol representation may therefore have a significant impact on the modelled optical depths over Europe. In northwestern Africa, mineral dust and biomass-burning aerosols are the main contributors to the observed optical depths. The fact that HadGEM2 underestimates the mineral dust optical depth has already been highlighted by the comparison against AeroCom models. As the tuning of the mineral dust scheme is not final in HadGEM2, the final version may improve the comparison in the region. Biomass-burning may also be underestimated due to a lack of transport from the agricultural fire region to the south of the AERONET

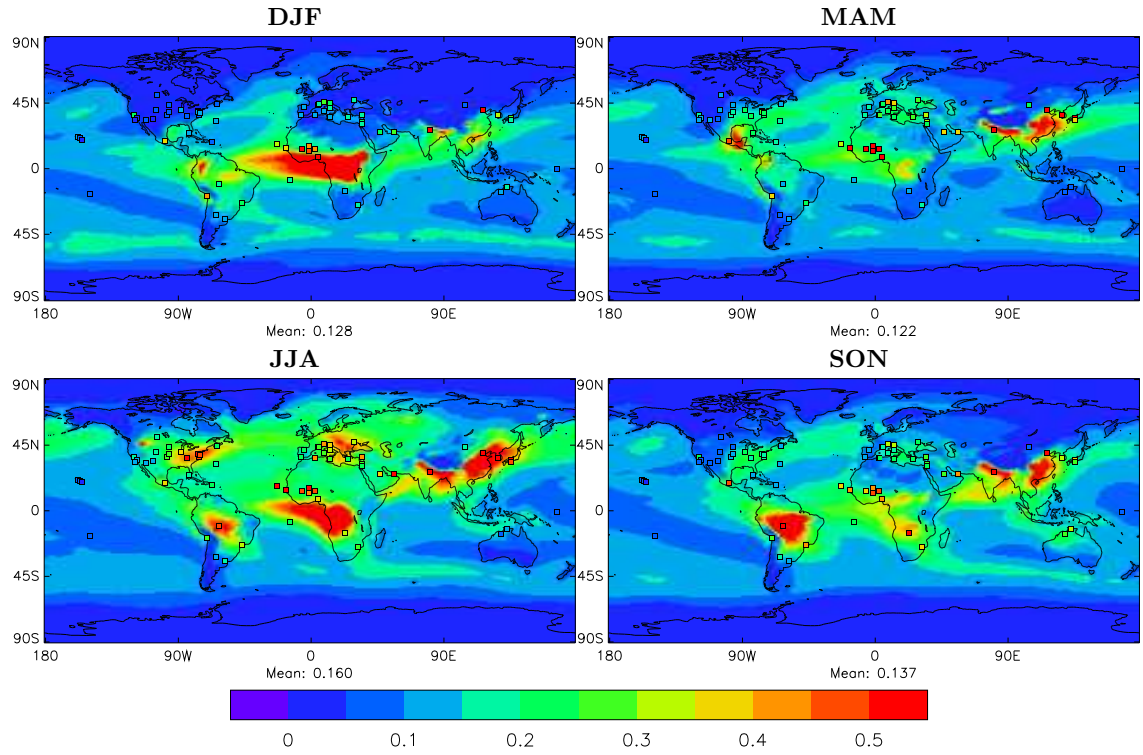

Figure 12: Seasonal distributions of the total aerosol optical depth at 0.44 μm as simulated by HadGEM2 (10-year means). Superimposed are multi-year seasonal means for selected AERONET sites.

sites.

6.2.2 Single-scattering albedo

The biomass-burning absorption properties were updated according to aircraft measurements. In HadGEM1, the single-scattering albedo had a value of 0.80 everywhere. In HadGEM2, the biomass-burning aerosol experiences hygroscopic growth and the single-scattering albedo varies across the globe. AERONET provides the opportunity to validate these changes. Table 5 shows the single-scattering at 0.55 μm for AERONET sites during their respective biomass-burning season [Dubovik *et al.* 2002]. The corresponding modelled value is taken from the grid-box containing the AERONET site. The observed single-scattering albedo is never as low as that used in HadGEM1. Aerosol absorption was therefore over-estimated in that model. In contrast, the revised scheme for HadGEM2 does a much better job. The absorption in Mongu, a site which is close to the fire and samples fresh biomass-burning aerosols, is under-estimated. It is interesting that the Canadian fire is well represented, despite the fact that the biomass-burning scheme was designed from aircraft observations in Africa.

6.3 Vertical profile of mineral dust and biomass-burning

Although AERONET measurements (and satellite retrievals) provide the opportunity to validate the columnar total aerosol optical depth, they say nothing about the verti-

Site	AERONET	HadGEM1	HadGEM2
Mongu, Zambia (15°S–23°E, Aug–Nov)	0.87 ±0.02	0.80	0.93
Amazonian forest (2°S–54°W, Aug–Oct)	0.94 ±0.02	0.80	0.92
Brazilian cerrado (15°S–56°W, Aug–Oct)	0.90 ±0.03	0.80	0.94
Canadian boreal forest (55°N–100°W, Jun–Sep)	0.94 ±0.02	0.80	0.93

Table 5: Aerosol single-scattering albedo at 0.55 μm as retrieved from AERONET sun-photometer measurements and the corresponding modelled value using the original (HadGEM1) and revised (as introduced for HadGEM2) schemes.

cal distribution of those aerosols. The vertical profile is important for both the direct and indirect effect. For the direct effect, the distribution of radiative fluxes within the atmosphere is affected by natural and anthropogenic aerosols. When quantifying the direct forcing due to anthropogenic aerosols, natural aerosols change the radiative fluxes experienced by the anthropogenic aerosols, and therefore their direct forcing. When the natural aerosol layer underlies the anthropogenic aerosol layer, the direct forcing is made less negative by the increase in the underlying surface brightness. When both aerosols are mixed together at the same altitude, this effect does not happen. Similarly, when anthropogenic aerosols are above bright clouds, their single-scattering albedo can reach the critical value and their direct effect switches sign. For the indirect effects, the importance of the vertical profile is more obvious. To exert indirect perturbations, aerosols must interact with clouds and therefore must be able to enter the cloud.

Aircrafts are able to measure the vertical distribution of the aerosol extinction by flying through the aerosol layer. The field campaign DABEX (Dust and Biomass Experiment) took place in January and February 2006 in Niger. It targeted the mixture of biomass-burning and mineral dust aerosols that is expected there on those months. The Met Office aircraft measured the vertical profile of the aerosol extinction (m^{-1}) at three wavelengths of the visible spectrum: 0.44, 0.55, and 0.70 μm. Biomass-burning aerosols being made of predominantly small particles, their extinction significantly depends on the wavelength. In constrast, mineral dust aerosols are mainly made of coarse particles which scatter radiation in an almost wavelength-independent way across the solar spectrum. It is therefore possible to separate the two aerosol layers and obtain the speciated vertical profiles shown on Figure 13. These profiles are an average of all profiles made during DABEX. Figure 13 also shows the corresponding profiles simulated by HadGEM2. As the comparison against AERONET measurements has shown that the aerosol optical depth is underestimated in the DABEX region, measured and modelled total extinction profiles have been normalised to 1 at 700 hPa and 0.55 μm. This comparison therefore focuses on whether the model places the two aerosol species at the right vertical locations, and whether the wavelength-dependence of their extinction is well simulated. On both points, the model does very well. The mineral dust layer is correctly located in the lower atmosphere, with small differences above 900 hPa. The mineral dust small wavelength dependence is also well reproduced, meaning that the mineral dust size distribution is sensible. The height of the biomass-burning plume is also very well simulated, with most of the extinction happening between 850 and 550 hPa, above the mineral dust layer. The

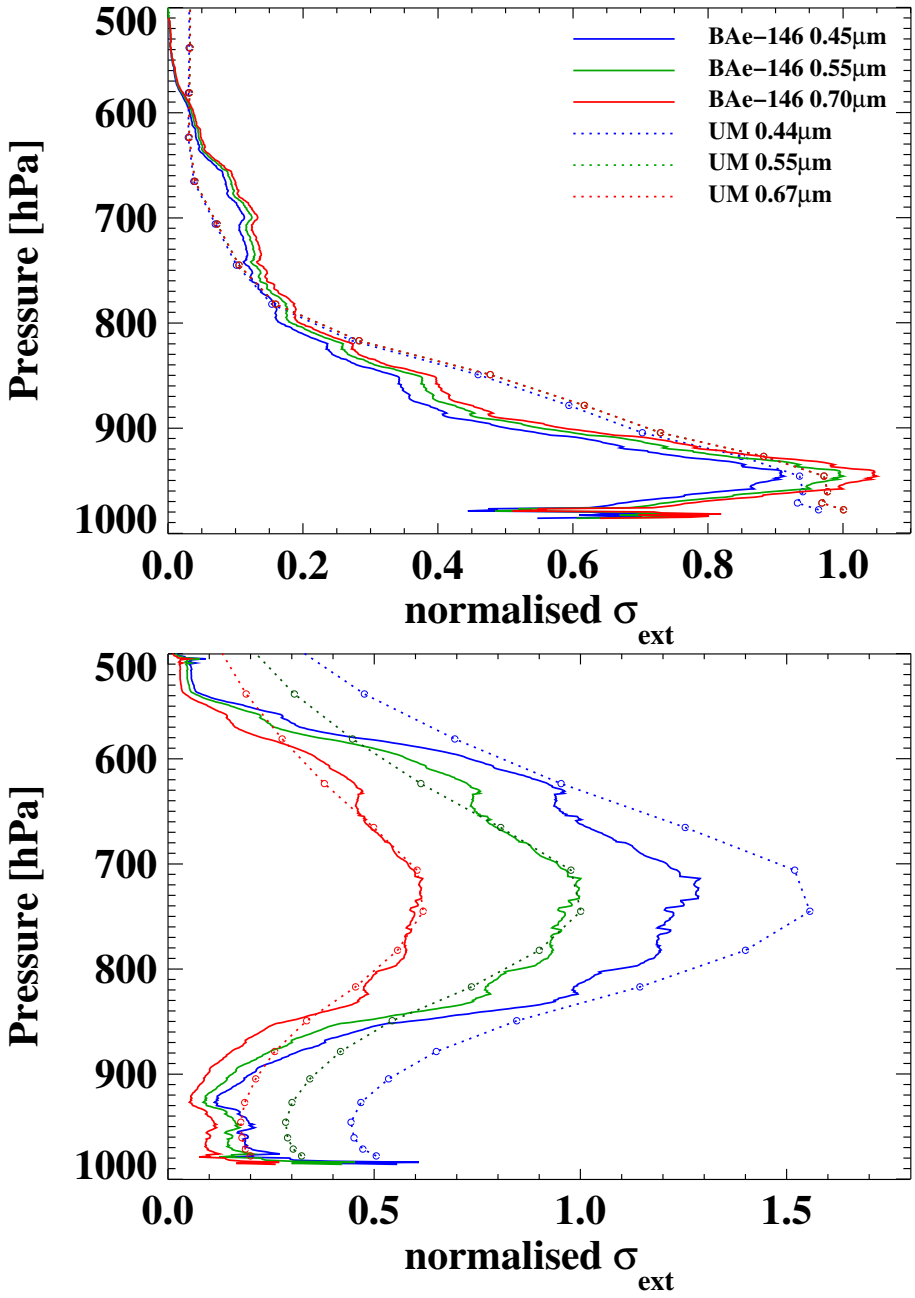

Figure 13: Vertical distribution of the normalised, wavelength-dependent extinction (σ_{ext} in m^{-1}) due to mineral dust (top) and biomass-burning (bottom) aerosols. Solid lines correspond to the average of all profiles taken by the Met Office aircraft during the DABEX campaign in Niger (January–February 2006). Dotted lines are the corresponding profiles simulated using the improved aerosol schemes in HadGEM2.

model matches the extinction at 0.55 and 0.7 μm, but overestimates that at 0.44 μm. This difference is due to assumptions in biomass-burning size distributions and absorbing properties.

6.4 Comparisons against satellite retrievals

6.4.1 MODIS and MISR

MODIS is the MODerate resolution Imaging Spectroradiometer. Two nominally identical versions of the instrument are currently operating onboard NASA's Terra (launched December 1999) and Aqua (launched May 2002) platforms. The instrument is characterised by a large number of spectral channels. This feature allows the implementation of advanced inversion algorithms for deriving the aerosol optical depth over oceans and dark land surfaces. Several products are available, including the aerosol optical depth at 0.55 μm. As with most other sensors, the MODIS aerosol algorithm cannot retrieve the total aerosol optical depth where the contribution of aerosols to the total signal is negligible compared to contributions of the surface and clouds. For this reason, only cloud-free areas are observed, and deserts and snow-covered areas are not included. Some areas may be subject to contamination by a wrongly corrected surface contribution or undetected clouds (especially thin cirrus). Remer *et al.* [2005] have validated the MODIS optical depth against in-situ measurements and identified biases over both land and ocean surfaces. The uncertainty $\Delta\tau$ in the measured optical depth, τ, is found to be $\Delta\tau = \pm 0.03 \ \pm 0.05\tau$ over ocean and $\Delta\tau = \pm 0.05 \ \pm 0.15\tau$ over land. A new version of the MODIS aerosol retrieval algorithm, called *collection 5*, has recently been issued and is used in this document. Changes are small over oceans, but the large optical depths observed over some land areas, such as the border of deserts and possibly undetected snow, are now much reduced.

MISR is the Multiangle Imaging SpectroRadiometer and is onboard the Terra platform. It is used to retrieve the aerosol optical depth at 0.55 μm. Its design allows for simultaneous observations in 9 viewing directions, therefore providing additional constrains when inverting the measured signal. This allows the removal of the Earth's surface contribution to the measured signal. MISR is therefore able to retrieve the aerosol optical depth over most cloud-free ocean and land surfaces, including deserts but excluding ice-covered areas. The downside of the instrumental design is the narrow swath of the instrument. Global coverage at the Equator is achieved every 9 days, compared to the 2 days needed by MODIS. The sampling of the aerosol burden by the two instruments is therefore not the same. Abdou *et al.* [2005] have shown that, over land, the MISR aerosol optical depth is smaller than that retrieved by MODIS collection 4. A comparison against AERONET ground-based measurements shows a better performance from MISR than MODIS, again hinting to the fact that MODIS collection 4 overestimates the aerosol optical depth over land surfaces. The collection 5 algorithm is expected to improve the comparison between the two satellite instruments. The different sampling may also play a significant role. Over ocean surfaces, both instruments are in a good agreement.

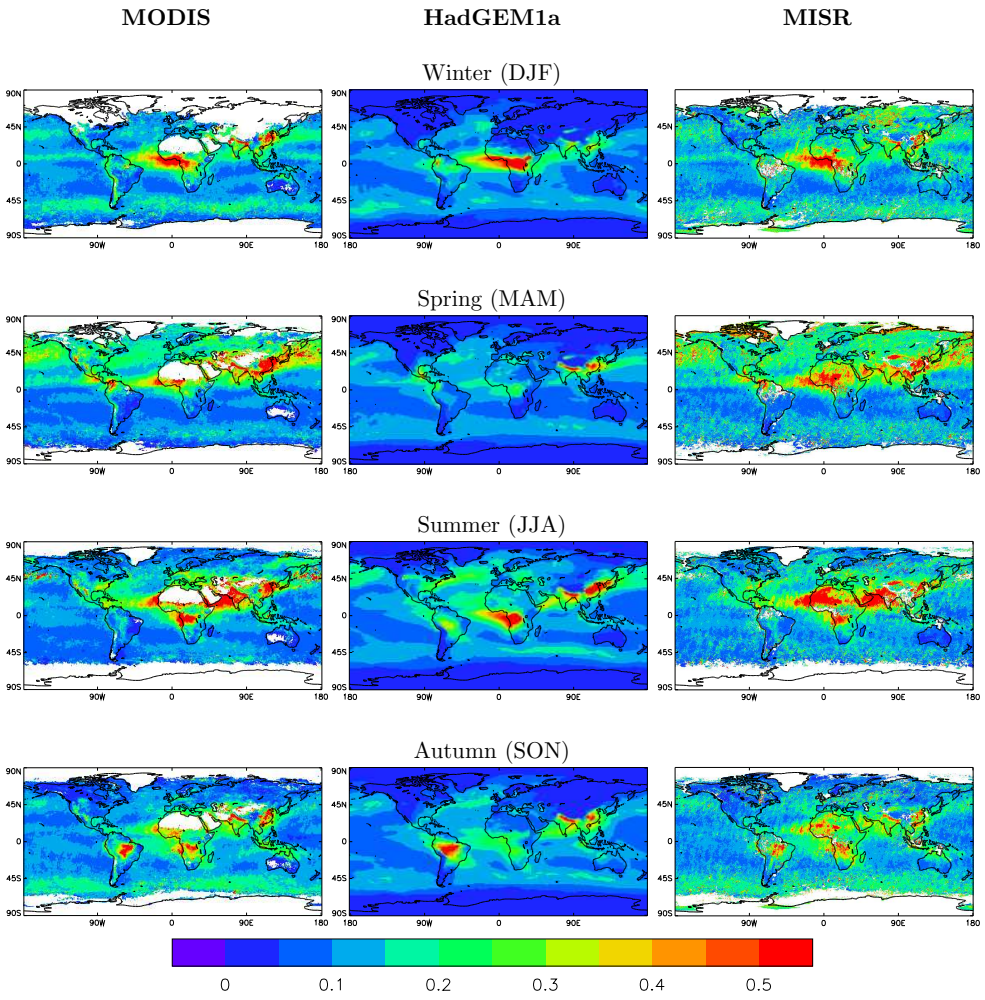

Figure 14: Seasonal distributions of the aerosol optical depth at 0.55 μm as observed by the MODIS and MISR satellite instruments in 2001 (left and right, respectively), and modelled by HadGEM1 for present-day conditions (centre). Seasons are those experienced by the Northern Hemisphere.

6.4.2 Seasonal distributions

Seasonal distributions of the total aerosol optical depth are shown in Figure 14 from the model (annual mean from a 1-year run including all available aerosols, using emissions for the year 2000), MODIS and MISR (observations for the year 2001). White areas in the satellite-derived distributions correspond to surfaces where retrieval is not attempted or to areas where the sun hasn't risen at the time of the satellite overpass. MODIS and MISR exhibit similar patterns. MODIS do not retrieve the aerosol optical depth over bright surface, such as deserts, and snow- or ice-covered surfaces. MISR is able to obtain retrievals over desert areas and snow-covered areas, although surface contamination may happen over the North Hemisphere continents in winter. The noisier MISR distribution is due to the instrument's narrow swath.

During the Northern-Hemisphere winter, the aerosol optical depth distribution is dominated by the strong signal due to the mixture of mineral dust and biomass-burning aerosols in Africa near the Equator. Sea salt is also an important contributor in the high latitudes of the Southern Hemisphere. HadGEM2 is able to reproduce

those two features quite well. However, the model lacks the moderate optical depths observed in North America and Europe. As already stated when comparing against the AERONET climatology, this is linked to missing sulphur dioxide oxidation by ozone and missing nitrate aerosols.

In spring, the transport of dust from China, mixed with industrial pollution, is clearly visible on the observed optical depth distributions. The model does simulate that particular transport, although at reduced optical depths. As 2001 seems to be have been an exceptional year on that aspect, the model underestimate is not especially an issue. In the Sahara and Saudi Arabia however, the mineral dust aerosol optical depths are underestimated by the current mineral dust scheme. The biomass-burning season in Africa, which is located north of the Equator, is also underestimated by the model.

In summer, satellite-derived distributions show different areas of large aerosol optical depths. In the Congo Basin, this is associated with biomass-burning aerosols. Industrial pollution aerosols are responsible with patterns over the United States, Europe, and China. HadGEM2 does a very nice job at simulating those events. On the other hand, the model does not reproduce the large optical depths associated with the transport of mineral dust across the Atlantic towards the Carribean. Here again, it is hoped that the final tuning of the mineral dust scheme will improve that aspect of the comparison.

In autumn, the biomass-burning and mineral dust seasons are ending in Africa, and the fire season is peaking in South America. Both events are simulated by the model, although the biomass-burning season in Africa seems to end too abruptly. Europe is once again associated with underestimated optical depths, even when compared to MISR.

These comparisons confirm the findings of the comparison against the AERONET climatology at a broader scale. The two main areas where the model does poorly are Europe in winter and northwestern Africa. However, the model also does a very good job in many other areas and is therefore very much in line with comparable global models that include aerosol representations [Kinne *et al.* 2006].

6.4.3 Zonal means

The direct aerosol radiative forcing is not maximum when the sun reaches the zenith, but for a solar zenith angle of about 70°. The exact value depends on the aerosol size distribution [Boucher *et al.* 1998] and absorbing properties. Consequently, the same aerosol at the same optical depth will be more efficient at exerting a direct effect when located at mid-latitudes than when located at the Equator. Being able to reproduce the observed zonal distributions of aerosols is therefore important. Figure 15 shows the annual-averaged zonal aerosol optical depth for all aerosols over both land and oceans (top panel), and for anthropogenic aerosols over oceans only (bottom panel). The latter uses results from the aerosol identification algorithm by Bellouin *et al.* [2005] applied to MODIS data for the year 2002. For the modelled optical depth, sulphate, biomass-burning and black carbon aerosols are considered as being entirely of anthropogenic origin.

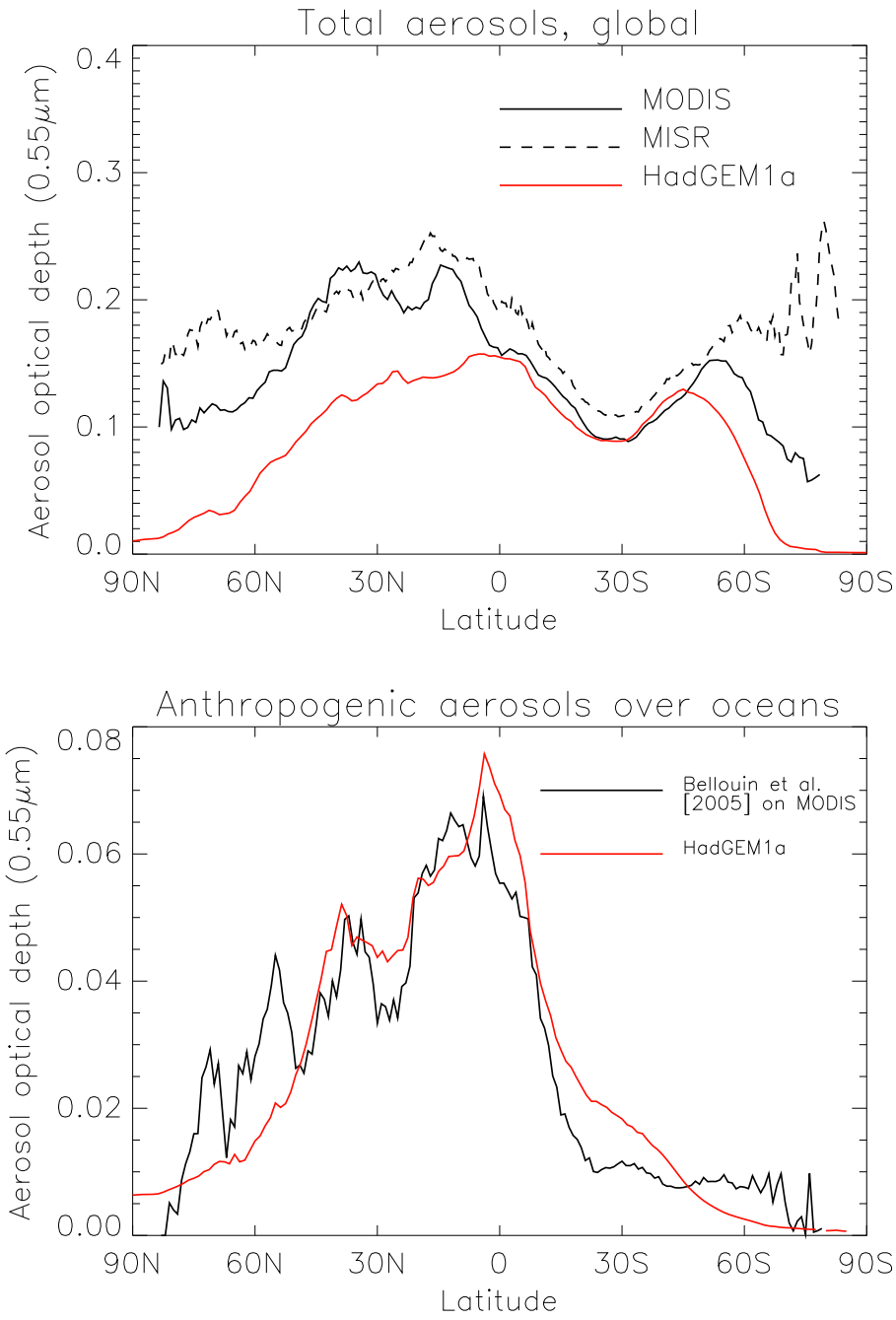

Figure 15: Top: Zonal means of the annual-averaged total aerosol optical depth at 0.55 μm over both land and ocean surfaces, as observed in 2001 by the MODIS and MISR satellite instruments (solid and dashed black lines, respectively) and simulated by HadGEM2 (red line). Bottom: Zonal means of the anthropogenic aerosol optical depth at 0.55 μm as estimated by Bellouin *et al.* from MODIS observations in 2002 (black line) and simulated by HadGEM2 (sulphate, biomass-burning and black carbon aerosols only). Modelled distributions use emissions for the year 2000.

Both satellite instruments are in overall agreement, expect at high latitudes in both hemisphere. In the Northern Hemisphere, MODIS is unable to retrieve aerosol properties over snow-covered surfaces whereas MISR retrieves significant values. It causes the MISR zonal average to be larger than that from MODIS. In the Southern Hemisphere, the relatively limited sampling of MISR is responsible for the noisy signal shown south of latitude 60°S. In a large band of latitudes spanning 20°N to 60°S, both instruments are in a very good agreement. The model is able to reproduce the general pattern of the observed zonal means although it doesn't succeed at matching the observed magnitudes. North of latitude 30°N, the optical depths are underestimated by a factor two. In the intertropical regions, the agreement with observations is satisfactory.

In order to estimate the direct forcing of the climate system due to the direct effect of anthropogenic aerosols, Bellouin *et al.* [2005] developed an algorithm able to identify the aerosol origin from several MODIS retrievals. Because of the limitations of the MODIS instrument, this algorithm is most efficient over ocean surfaces. The zonal means of the bottom panel of Figure 15 are therefore limited to ocean surfaces. The agreement between the model and the estimates by Bellouin *et al.* [2005] is impressive. The transport of anthropogenic aerosols emitted in the model performs well. It must be noted, however, that the anthropogenic optical depth by Bellouin *et al.* [2005] has its own uncertainty and our successful comparison could arguably be considered as a validation of their identification algorithm.

6.4.4 Cloud droplet effective radius

Validation of the indirect effects exerted by modelled aerosols on cloud droplet size distributions is more difficult. There exists however satellite retrievals of the cloud droplet effective radius (r_e). Since satellite observe the Earth from above, that radius is that of the droplets at the top of the cloud; HadGEM can diagnose the same quantity. Figure 16 shows satellite retrievals by Han *et al.* [1994] and Kawamoto [1999]. They both use four months (January, April, July, October) of observations by the Advanced Very High Resolution Radiometer (AVHRR) satellite instrument for the year 1987. Despite using the same data, there are significant differences between the satellite retrievals, so it is difficult to draw detailed quantitative conclusions. The results show the considerable increase in r_e that was previously reported in table 2. For example, over large parts of the Southern Hemisphere, r_e has increased from around 12 μm to around 16 μm. Whereas HadGEM1 displays results that seem too low compared with the retrievals, the results from the improvements included in the prototype of HadGEM2 now appear to be too large.

7 Conclusions

The representations of aerosols in the Hadley Centre climate model have been improved significantly. Specifically, changes have been made to the sulphate and biomass-burning aerosol schemes, mineral dust and secondary organic aerosols have been added, and diagnostics now allow the comparison of simulated aerosol optical depths against those measured *in-situ* or by remote-sensing techniques.

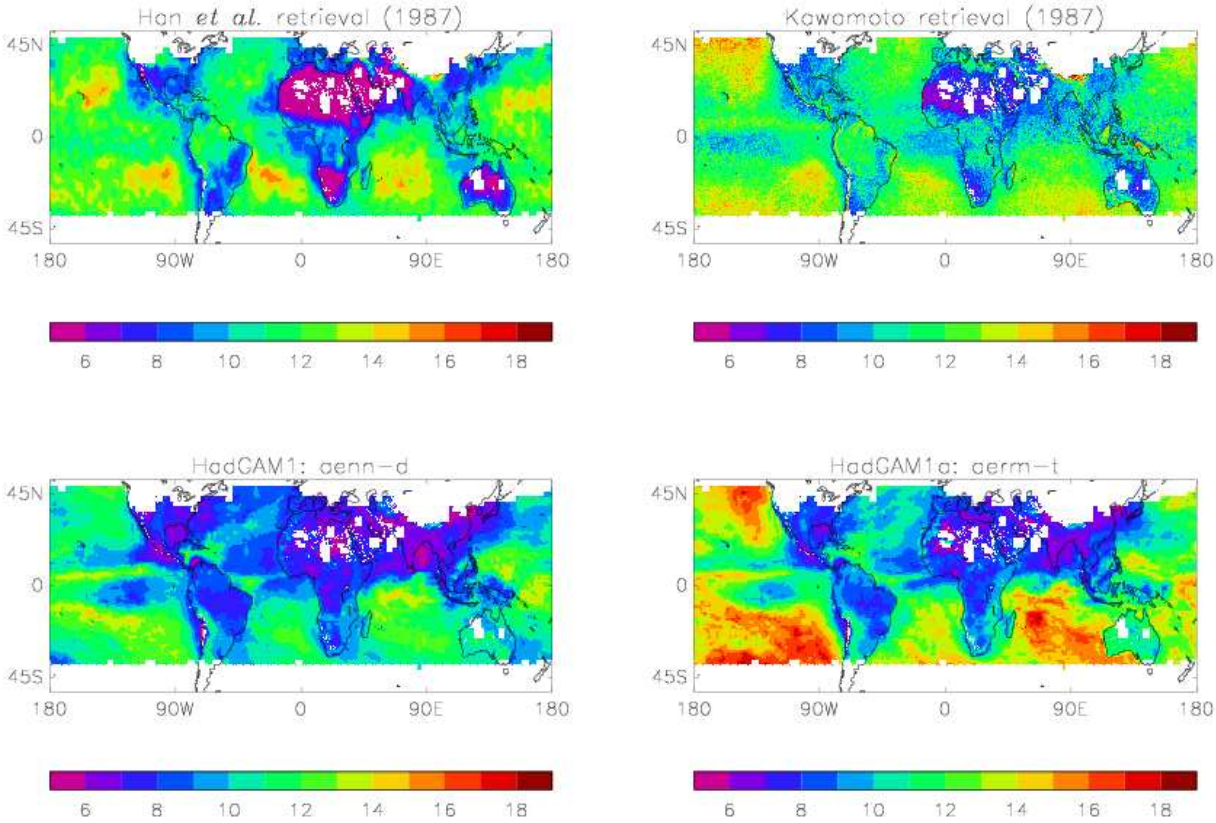

Figure 16: Distributions of the 4-month averaged cloud droplet effective radius as retrieved by Han *et al.* [1994] and Kawamoto [1999] from AVHRR data for 1987, and as simulated by HadGEM1 and a prototype of HadGEM2 including improved aerosols.

The sulphate mass now lies mostly in the optically-efficient accumulation mode. This translates into a dramatic increase in the sulphate aerosol optical depth, and also in much more realistic times of residence within the atmosphere. This correction also allows the removal of inconsistent assumptions in the implementation of the indirect effect. The biomass-burning scheme has been improved according to an extensive set of observations during dedicated field campaigns (including measurements by the Met Office aircraft). Improvements were made to the emission dataset, aerosol ageing, and absorbing and hygroscopic properties. The biomass-burning representation is also now consistent with it exerting an indirect effect. Two important natural aerosol species, mineral dust and secondary organic aerosols, were also added to the model. Results for the mineral dust scheme presented here are from a developmental version of the scheme and show that a broadly realistic pattern of dust loading can be produced. Further modifications and tuning will improve dust simulations.

The comparison against several sources of observational data shows an overall good performance from the improved aerosol representations. There are areas where the model shows deficiencies, such as Europe in winter and northwestern Africa during mineral dust and biomass-burning events. But the model performs really well in simulating aerosol optical depths over many areas of the world, and the vertical distribution of dust and biomass-burning in Niger compares successfully against aircraft observations. The revised biomass-burning absorption matches more closely the retrievals from ground-based sun-photometers. The model is also in general agreement with comparable global models which include aerosol representations.

Including all improvements, aerosols in the HadGEM2 model exert a direct radiative forcing of -0.13 Wm^{-2} and a total (direct + indirect) forcing of -1.22 Wm^{-2} with respect to pre-industrial times.

8 References

References

[1] Abdou, W.A. *et al.* Comparison of coincident Multiangle Imaging Spectroradiometer and Moderate Resolution Imaging Spectroradiometer aerosol optical depths over land and ocean scenes containing Aerosol Robotic Network sites. *J.Geophys.Res.*, **110**, doi:10.1029/2004JD004693, 2005.

[2] Abel, S.J., Haywood, J.M., Highwood, E.J., Li, J., and Buseck, P.R. Evolution of biomass-burning aerosol properties from an agricultural fire in southern Africa. *Geophys. Res. Lett.*, **30**, doi:10.1029/2003GL017342, 2003.

[3] Andreae, M.O., Jones, C.D., and Cox, P.M. Strong present-day aerosol cooling implies a hot future. *Nature*, **435**, 1187–1190, 2005.

[4] Barrie, L.A. *et al.* A comparison of large-scale atmospheric sulphate aerosol models (COSAM): Overview and highlights. *Tellus*, **53B**, 615–645, 2001.

[5] Bahreini, R., *et al.* Measurements of secondary organic aerosol from oxidation of cycloalkenes, terpenes, and m-xylene using an Aerodyne aerosol mass spectrometer. *Environ. Sci. Technol.*, **39**, 5674–5688, 2005.

[6] Bellouin, N, Boucher, O., Haywood, J.M., and Reddy, M.S. Global estimate of aerosol direct radiative forcing from satellite measurements. *Nature*, **438**, 1138–1141, 2005.

[7] Boucher, O. *et al.* Intercomparison of models representing direct shortwave radiative forcing by sulfate aerosols. *J.Geophys.Res.*, **103**, 16979–16998, 1998.

[8] Cahill, T. M., V. Y. Seaman, M. J. Charles, R. Holzinger, and A. H. Goldstein. Secondary organic aerosols formed from oxidation of biogenic volatile organic compounds in the Sierra Nevada Mountains of California. *J. Geophys. Res.*, **111**, D16312, doi:10.1029/2006JD007178, 2006.

[9] Chan, M.N., and Chan, C.K. Hygroscopic properties of two model humic-like substances and their mixtures with inorganics of atmospheric importance. *Environ. Sci. Technol.*, **37**, 5109–5115, 2003.

[10] Davison, P.S., Roberts, D.L., Arnold, R.T., and Colvile, R.M. Estimating the direct radiative forcing due to haze from the 1997 forest fires in Indonesia. *J. Geophys. Res.*, **109**, doi:10.1029/2003JD00424, 2004.

[11] Dentener, F. *et al.* Emissions of primary aerosol and precursor gases in the years 2000 and 1750, prescribed data-sets for AeroCom. *Atmos. Chem. Phys.*, **6**, 4321–4344, 2006.

[12] Derwent, R.G., Collins, W.J., Jenkin, M.E., Johnson C.E., and Stevenson D.S. The global distribution of secondary particulate matter in a 3D Lagrangian chemistry transport model. *J. Atmos. Chem.*, **44**, 57–95, 2003.

[13] Dubovik, O. *et al.* Variability of absorption and optical properties of key aerosol types observed in worldwide locations. *J. Atmos. Sci.*, **59**, 590–608, 2002.

[14] Fitzgerald, J.W. Approximation formulas for the equilibrium size of an aerosol particle as a function of its dry size and composition and the ambient relative humidity. *J. Appl. Meteorol.*, **14**, 1044–1049, 1975.

[15] Ginoux, P. *et al.* Evaluation of aerosol distribution and optical depth in the GFDL coupled model CM2.1 for present climate. *J. Geophys. Res.*, **111**, D22210, doi:10.1029/2005JD006707, 2006.

[16] Han, Q., Rossow, W.B., and Lacis, A.A. Near-global survey of effective droplet radii in liquid water clouds using ISCCP data. *J. Clim.*, **7**, 475–497, 1994.

[17] Haywood, J.M. *et al.* The mean physical and optical properties of regional haze dominated by biomass-burning aerosol measured from the C-130 aircraft during SAFARI 2000. *J. Geophys. Res.*, **108**, doi:10.1029/2002JD002226, 2003.

[18] Iversen, J.D., and White, B.R. Saltation threshold on Earth, Mars and Venus. *Sedimentology*, **29**, 111–119, 1982.

[19] Janicke, R. Tropospheric aerosols, in *Aerosol-Cloud-Climate Interactions*, edited by P.V. Hobbs, Academic Press, San Diego, California, pp 1–31, 1993.

[20] Jones, A., Roberts, D.L., Woodage, M.J., and Johnson, C.E. Indirect sulphate aerosol forcing in a climate model with an interactive sulphur cycle. *J. Geophys. Res.*, **106**, D17, 20293–20310, 2001.

[21] Kawamoto, K. On the global distribution of the water cloud microphysics derived from AVHRR remote sensing. *Cent. Clim. System Res. Rep. 11*, Univ. of Tokyo, Tokyo, Japan, 1999.

[22] King, M.D., Kaufman, Y.J., Tanré, D., and Nakajima, T. Remote sensing of tropospheric aerosols from space: Past, present, and future. *Bull. Amer. Meteorol. Soc.*, **80**, 2229–2259, 1999.

[23] Kinne, S. *et al.* An AeroCom initial assessment - optical properties in aerosol component modules of global models. *Atmos. Chem. Phys.*, **6**, 1815–1834, 2006.

[24] Liu, L., Lacis, A.A., Carlson, B.E., Mishchenko, M.I., and Cairns, B. Assessing GISS ModelE aerosol climatology using satellite and ground-based measurements: A comparison study. *J. Geophys. Res.*, **111**, D20212, doi:10.1029/2006JD007334, 2006.

[25] Lund-Myhre, C., and Nielsen, C.J. Optical properties in the UV and visible spectral region of organic acids relevant to tropospheric aerosols. *Atmos. Chem. Phys.*, **4**, 1759–1769, 2004.

[26] Magi, B.I. and Hobbs, P.V. Effects of humidity on aerosols in southern Africa during the biomass burning season. *J. Geophys. Res.*, **108**, doi:10.1029/2002JD002144, 2003.

[27] Penner, J.E., *et al.* Model intercomparison of indirect aerosol effects. *Atmos. Chem. Phys.*, **6**, 3391–3405, 2006.

[28] Ramaswamy, V. *et al.* Radiative forcing of climate change, in *Climate Change 2001: The Scientific Basis*, edited by Houghton, J.T., *et al.*, Cambridge University Press, Cambridge, United Kingdom, 2001.

[29] Reddy, M.S. *et al.* Estimates of global multicomponent aerosol optical depth and direct radiative perturbation in the LMD general circulation model. *J. Geophys. Res.*, **110**, D10S16, doi:10.1029/2004JD004757, 2005.

[30] Remer, L. A. *et al.* The MODIS aerosol algorithm, products and validation. *J. Atmos. Sci.*, **62**, 947–973, 2005.

[31] Roberts, D.L. and Jones, A. Climate sensitivity to black carbon aerosol from fossil fuel combustion. *J. Geophys. Res.*, **109**, D16202, doi:10.1029/2004JD004676, 2004.

[32] Schulz, M. *et al.* Radiative forcing by aerosols as derived from the AeroCom present-day and pre-industrial simulations. *Atmos. Chem. Phys.*, **6**, 5225–5246, 2006.

[33] Spracklen, D.V., Pringle, K.J., Carslaw, K.S., Chipperfield, M.P., and Mann, G.W. A global off-line model of size-resolved microphysics: 1. Model development and prediction of aerosol properties. *Atmos. Chem. Phys.*, **5**, 2227–2252, 2005.

[34] Stier, P. *et al.* The aerosol-climate model ECHAM5-HAM. *Atmos. Chem. Phys.*, **5**, 1125–1156, 2005.

[35] Stott, P.A., Tett, S.F.B., Jones G.S., Allen, M.R., Mitchell, J.F.B., and Jenkins, G.J. External control of twentieth century temperature by natural and anthropogenic forcings. *Science*, **290**, 2133–2137, 2000.

[36] United Nations. *The World at Six Billion*, Population Division, Dept. of Economic and Social Affairs, United Nations Secretariat, New York, 1999.

[37] Varutbangkul, V., *et al.* Hygroscopicity of secondary organic aerosols formed by oxidation of cycloalkenes, monoterpenes, sesquiterpenes, and related compounds. *Atmos. Chem. Phys.*, **6**, 2367–2388, 2006.

[38] Woodward, S. Modelling the atmospheric life cycle and radiative impact of mineral dust in the Hadley Centre climate model. *J. Geophys. Res.*, **106**, D16, 18155–18166, 2001.